論文題目 (Title of Thesis)：

In vivo brain imaging for synapse remodeling in developing mouse cortex and its application to the analysis of autism model mice

(発達期大脳皮質シナプスリモデリングの in vivo 観察と自閉症モデルマウスへの応用)

氏　　名 (Name)：　一色　真明　(Isshiki Masaaki)

追加情報(Additional information)：

この論文に含まれる内容は以下のように出版されています。

The contents in this article were published as follows.

Isshiki M., Tanaka S., Kuriu T., Tabuchi K., Takumi T. and Okabe S., Enhanced synapse remodelling as a common phenotype in mouse models of autism. Nature Communications. 2014 Aug 21, 5:4742.

DOI:　10.1038/ncomms5742

URL:　http://www.nature.com/ncomms/2014/140821/ncomms5742/full/ncomms5742.html

博士論文

論文題目　*In vivo* brain imaging for synapse remodeling in developing mouse cortex and its application to the analysis of autism model mice

（発達期大脳皮質シナプスリモデリングの

*in vivo*観察と自閉症モデルマウスへの応用）

氏　名　　一色　真明

Table of contents

1. Abstract

Early studies of synapse dynamics in cell culture preparations indicated that the dynamic balance between gain and loss of synapses underlies gradual increase of synapse density. Existence of similar kinetic properties of synapse dynamics may exist *in vivo,* but previous *in vivo* studies with two-photon microscopy in the mature neocortex indicated highly stable nature of mature spines. Extensive remodeling of synapses in culture preparations may reflect properties of early neuronal circuits *in vivo*. Alternatively, it may be caused by artificial environment of cell culture. To clarify this point, we applied *in vivo* two-photon time-lapse imaging to the mouse cortex during postnatal development and visualized both changes in spine morphology and gain and loss of the postsynaptic densities. Our study revealed extensive remodeling of spines with postsynaptic specialization and importance of the balance between gain and loss of spine synapses in the regulated increase of synapse density in the early postnatal period.

Developmental deficits in neuronal connectivity are proposed to be present in patients with autism spectrum disorders (ASDs). In the second part of our thesis, we examined this possibility using *in vivo* imaging of synapses in the early postnatal cortex of three ASD mouse models with distinct genetic backgrounds. The first mouse model is genetically engineered mice with chromosome duplication, mimicking human

15q11-13 copy number variation (CNV). The second mouse model is knock-in mice containing meuroligin-3 R451C point mutation, detected as a rare variant in families with multiple ASD patients. The third model is the inbred strain BTBR mice showing typical deficits in social behaviors. These mice showed consistent upregulation in the dynamics of PSD-95-positive spines, which may subsequently contribute to stable synaptic connectivity. Meanwhile, spines receiving inputs from the thalamus, detected by the presence of gephyrin clusters, were larger, highly stable, and unaffected in ASD mouse models. Importantly, the three distinct mouse models showed highly similar phenotypes in spine dynamics. This selective impairment in dynamics of PSD-95-positive spines receiving intracortical projections may be a core component of early pathological changes and therefore a potential target of early intervention.

List of abbreviation

PSD	postsynaptic density
ASD	autism spectrum disorders
PND	postnatal day
VPM	ventral posteromedial nucleus
POm	medial posterior nucleus
TCA	thalamocortical axon
CNV	copy number variation
GABA	gamma-aminobutyric acid
SSC	somatosensory cortex
AFC	anterior frontal cortex
2PLSM	2-photon laser scanning microscopy
mIPSC	miniature inhibitory postsynaptic current

2. Introduction

Synapse imaging in postnatal developmental brain by *in vivo* two-photon microscopy

Complex neuronal networks in our brain serve a wide variety of functions. During the development of the vertebrate brain, neurons extend axonal processes to distant target regions and recognize their synaptic partners by multiple mechanisms including cell surface recognition and reception of trophic factors. After target recognition, the process of synapse formation and remodeling is initiated. This process is important for the establishment of diverse brain functions, especially for those require activity-dependent shaping of the immature circuits. Real-time monitoring of neuronal connectivity *in vivo* is an important strategy for understanding the mechanisms underlying brain development[1,2], functional maturation[3], and dysfunction[4]. Two-photon microscopy enabled researchers to resolve dendritic spines filled with GFP in the neocortex of living mice with time intervals of several days to months[5,6]. Initial studies revealed that more than 90% of spines imaged in the adult mouse neocortex were highly stable for several days and months[5]. A recent report indicated that motor learning enhances spine dynamics. This enhancement was proposed to be associated with functional alterations in neuronal circuits involved in motor coordination.[7]. However, highly stable nature of spines in the mature neocortex of mice contrasts with rapid turnover of synapses in culture conditions. There are two possibilities that can explain this discrepancy. First, synapse dynamics may be artificially upregulated by the presence or absence of exogenous factors in culture. Second, rapid synapse dynamics *in vitro* may reflect the state of synapses in the early phase of neural circuit development *in vivo*. In fact, synapses in the developing rodent neocortex were reported to increase 7-fold from postnatal day (PND) 6 to PND 21[8]. To discriminate these possibilities, we performed in vivo two-photon microscopy in the early postnatal period. At this stage of development, a substantial fraction of dendritic protrusions lack synaptic contacts[9]. To reliably detect spine synapses in immature neurons, we imaged both morphology of spines and accumulation of postsynaptic density (PSD) proteins tagged with GFP simultaneously[10]. This approach enabled us to discriminate dynamic filopodia, immature spines without PSD specialization, and spine synapses with accumulation of PSD proteins. Thus the precision of synapse detection in this study increased substantially.

Properties of local neural connectivity should be understood in the context of global architecture of the neural circuit. In the case of rodent somatosensory cortex, the sensory signals originated from the sensory neurons reside within the trigeminal ganglion are transmitted to the nuclei in the medulla oblongata, and then reach the thalamus[11]. With preserved somatotopy, axons of the thalamic neurons project to the somatosensory cortex. Sensory information related to the movement of vibrissae is processed in the ventral posteromedial nucleus (VPM) of the thalamus and the axonal projections from VPM form dense synaptic connections with layer IV stellate neurons[12,13]. In addition, distinct tactile information is relayed through the medial posterior nucleus (POm) of the thalamus and finally reaches pyramidal neurons in the layer 2/3 and layer 5/6[12,14]. These projections from the thalamus to the cortex (thalamocortical axons; TCAs) may have distinct properties in comparison with intracortical connections, such as projections from layer 4 stellate cells to layer 2/3 pyramidal neurons. A previous electron microscopic study indicated that a subset of spines in cortical pyramidal neurons receives inhibitory inputs from local interneurons and these spines selectively receive excitatory inputs from the TCAs[15]. In the present study, we aimed to detect dynamics of postsynaptic specializations receiving inputs from either other cortical neurons or thalamic neurons by specific labeling of a subset of spines with an inhibitory postsynaptic marker, GFP-tagged gephyrin.

Detection of the synaptic pathology of autism spectrum disorders in postnatal

development

Autism spectrum disorders (ASDs) are estimated to be closely tied to neuronal development and connection. Cortical dysfunction is considered to underlie deficits in social behaviors and communication in ASDs[16]. Symptoms of ASDs manifest during early development. Because of recent advances in early screening, ASDs can be reliably diagnosed by 3 years of age. Neuropathological studies of patients with ASD indicated relatively small changes in brain architecture and few signs of neurodegeneration[17]. The early onset of this disease and small pathological changes in the brain of patients with ASD led to the hypothesis that impairment in synapse formation, neuronal connectivity, and circuit stabilization may explain the pathogenesis of ASDs[18–20].

In agreement with the abovementioned concept, genetic studies of copy number variants (CNVs) and specific gene mutations have supported the hypothesis that nonsyndromic ASDs can be caused by structural or sequence variations in genes related to synapse development, including genes encoding cell adhesion and scaffolding molecules[21–23]. Furthermore, mouse molecular genetics confirmed an impairment of synaptic functions, including GABA signaling and long-term potentiation/depression, in multiple ASD mouse models[23–30]. Although these studies provide strong evidence that support a causal relationship between ASD-related gene mutations and synapse pathology, little is known about synapse formation and remodeling in the developing neocortex of these mouse models. Because ASD symptoms manifest during the early stages of cortical development, detection of impairment in synapse formation, stability, and remodeling will provide essential information in identifying core circuit-level defects at the onset of the disease.

A wide heterogeneity exists among patients with ASDs, and defining the core characteristics of this disease is very difficult from only the presentation of symptoms. To define the core characteristics of ASDs, neurobiological studies of mouse models and subgrouping based on genetic evidence are essential. Research on several diseases comorbid with autism have provided models linking defects in intracellular signaling with dysfunctions of synapses. Rett syndrome, fragile X syndrome, and tuberous sclerosis complex exhibit comorbidity with ASDs and their corresponding mouse models were established and extensively studied[31–34]. Rescue experiments using these syndromic ASD mouse models successfully identified key molecular pathways involved in the pathology of neural circuits and behavioral deficits[24,27,30,35–37]. However, most ASD cases are nonsyndromic, and recent genetic studies of nonsyndromic ASDs identified a large number of candidate rare genetic variants[21,22]. These studies revealed the important roles of both rare mutations and CNVs in the etiology of ASDs.

Interestingly, rare variants in genes of postsynaptic neuroligin-3 and -4 (*NLGN 3 and 4*) as well as their presynaptic binding partner neurexin-1 (*NRXN*1) have been linked with ASDs[23]. These findings suggest that the interaction between pre- and postsynaptic membranes have important roles in nonsyndromic ASDs. Among a variety of CNVs detected in ASDs, duplication of 15q11–13 has been most frequently reported, suggesting that the dosage of one or more genes in this chromosomal region is critical for normal brain function[38]. To extract common neurodevelopmental defects in nonsyndromic ASDs, comparison of mouse models that mimic rare mutations in neuroligin and chromosomal duplication in 15q11–13 may provide indispensable information. Therefore, we characterized the two following types of nonsyndromic ASD mouse models: patDp/+ mice[39], which mimic human chromosome 15q11–13 duplication, and NLG R451C mice[29], which are engineered to have a rare missense mutation of *Nlgn3* similar to that of patients with ASD in this study. Additionally, we analyzed BTBR T+tf mice as the third nonsyndromic ASD model mice. BTBR T+tf (Black and Tan BRachyury) mice are an inbred strain that carries the mutations *T* (brachyury) and $Itpr3^{tf}$ (inositol 1,4,5-triphosphate receptor 3; tufted)[40,41]. BTBR mice exhibit behavioral phenotypes that mimic all three diagnostic symptoms of ASD, deficit in social interaction, abnormal communication and repetitive behavior[42]. However the synaptic phenotypes in the postnatal development are little known.

We performed *in vivo* two-photon time-lapse imaging in developing layer 2/3 pyramidal neurons expressing GFP-tagged synaptic markers, PSD-95 and gephyrin, and the red fluorescent protein DsRed2. Dendritic spines with PSD-95 clusters showed enhanced turnover in patDp/+, NLG R451C and BTBR mice. Spines receiving input from the thalamus that were detected by the presence of gephyrin clusters were larger, highly stable, and unaffected in patDp/+ and NLG R451C mice. Thus, spines containing PSDs and receiving intracortical projections were consistently affected in the developing cortex of two nonsyndromic ASD mouse models. This selective impairment in synaptic dynamics may be a core component of early pathological changes at the onset of ASDs and a possible target of early intervention for the disease.

3. Materials and Methods

Animals and constructs

All experimental procedures were performed in compliance with the institutional guidelines of the University of Tokyo. Male or female wild-type ICR (Fig. 1-4) and C57Bl/6J (Fig. 5 and 6) mice (Japan SLC. Inc.) were used for *in vivo* imaging. Male of the following ASD mouse models were used in this study: patDp/+ mice with paternal duplication of chromosome 7c[39], NLG R451C mice with a point mutation corresponding to the human neuroligin-3 R451C[29] and BTBRT+tf mice[42]. The patDp/+ and the NLG R451C mice strains were kindly supplied by Prof. Toru Takumi and Prof. Katsuhiko Tabuchi, respectively. The BTBRT+tf mouse strain (RBRC 01206) was provided by RIKEN BRC through the National Bio-Resource Project of the MEXT, Japan. Constructs of PSD-95-GFP were previously described[43]. An expression plasmid of DsRed2 was constructed by replacing the cDNA sequence from pDsRed2-N1 (Clontech) with GFP of pAct-GFP. An expression plasmid for gephyrin-GFP was constructed by inserting the gephyrin-GFP fragement[44] into the pCAGGS vector. PSD-95-GFP and DsRed2 were expressed under the control of the β-actin promoter, and gephyrin-GFP was expressed under the control of the CAG promoter.

In utero electroporation

Progenitor cells of layer 2/3 neurons in the SSC and AFC were transfected using *in utero* electroporation[45,46]. E15.5 timed pregnant mice were deeply anesthetized with an intraperitoneal injection of pentobarbital (100 mg/kg), and the uterine horns were exposed. Approximately 1 µl of DNA solution [a mixture of DsRed2 plasmid (1 µg/µl) with either a PSD-95-GFP plasmid (1–2 µg/µl) or a gephyrin-GFP plasmid (0.1 µg/µl)] was pressure-injected into the lateral ventricle of each embryo through a pulled-glass micropipette. The head of each embryo was placed between tweezer-type electrodes (CUY650P5, NEPA Gene). Square electric pulses (28–33 V, 50 ms) were passed four times at 1 Hz using an electroporator (CUY21, NEPA Gene).

Surgery for *in vivo* imaging

We applied the thinned-skull technique[47–49] to most of the *in vivo* two-photon imaging. Thinned-skull windows were prepared by carefully thinning a small circular area of the cranium by micro surgical blades to approximately 15 µm thickness. Mice expressing fluorescent proteins at postnatal weeks 1–8 were anesthetized with intraperitoneal injections of ketamine (100 mg/kg body weight) and xylazine (10 mg/kg body weight). For juvenile mice, the dose of anesthesia was reduced to half. Minimum doses of ketamine and xylazine were arbitrarily administered as supplemental anesthesia. The skull was exposed by incising a midline of the scalp. A small metal pipe (diameter, 3 mm) was glued to the skull with dental cement (Sunmedical). Mice were held on a stereotaxic instrument using the pipe. The surface compact bone and the intermediate spongy bone were removed with the help of a spherical drill bit (Fine Science Tools) attached to a hand-held high speed drill until the thickness of the remaining bone reached approximately 50 µm. Further thinning was manually performed using micro surgical blades (NORDLAND blade, Salvin Dental) until that part of the skull was approximately 15 µm in thickness. Care was taken to not push the skull during the thinning process to avoid brain damage. The imaging locations were as follows: SSC, bregma −1.0/−1.5 mm and lateral 1.5–2.5/2.0–3.0 mm (young/adult); AFC, bregma 2.1–3.0 mm and lateral 0.8–1.4 mm (Fig. 9).

The thinned-skull technique cannot be applied to mice younger than PND 20. In young animals, deterioration of the point-spread function through the thinned-skull window was severe, probably because of the immature spongy bone tissue of the cranium. Because the collection of synaptic dynamics data in young animals was necessary in some sets of experiments (Fig. 1-4 and 10), we switched to the open-skull window technique in these cases[48]. Our comparisons of the two techniques indicated that the open-skull window technique can reliably report synaptic dynamics when great care was taken to prevent the activation of glia in the surgical area. We previously reported that the resolution of 2PLSM is comparable with two cranial window preparations in the superficial layer of the neocortex[50]. The surgical procedures for open-skull windows are as follows. A circular groove was made on the skull with a trephine (2.3 mm in diameter, Fine Science Tools) attached to a high-speed drill. The central island of the skull bone was carefully lifted using a microprobe and forceps with the underlying dura intact. The cranial window was covered with a sterile 3 mm coverglass and sealed with dental cement. We evaluated the surgical procedures of individual experimenters by scoring multiple parameters, including the total operation time, bleeding from the bone tissue, brain swelling, intact brain surface after bone removal, bleeding from the dura, and cleanliness of the glass window after application of the adhesive. Only if all the scores were very good, the surgery was judged as successful.

In vivo imaging

After surgery, mice were immediately placed under a scanning microscope (FV300, Olympus) equipped with a pulsed laser (MaiTai HP, Spectra Physics) and a water immersion objective lens (1.05 NA, 25×, Olympus). To concurrently obtain GFP and DsRed2 signals, the wavelength was set to 920 nm, and the average power of the laser after the objective lens was approximately 20 mW. GFP and DsRed2 fluorescence signals were separated with a dichroic mirror (550 nm) and barrier filters (515/30; 575IF). The imaging area was 565 × 565 μm (low magnification) or 78 × 78 μm (high magnification), and the step size of the z stack was set to 2 or 0.75 μm. The pixel sizes of single horizontal images were set to 512 × 512. Imaging depth was <100 μm from the pia. Apical dendritic branches in layer 2/3 pyramidal neurons were randomly selected for analyses. We recorded the brain vasculature pattern using a CCD camera (GZ-MG70, Victor) to create vasculature maps, which facilitated the identification of the imaged area in previous sessions. After an imaging session, the scalp of mice with thinned-skull windows was sutured. Mice before weaning (younger than postnatal week 2) were housed with their littermates and mothers between imaging sessions. Mice after weaning (older than postnatal week 3) were individually housed between imaging sessions. Intervals of *in vivo* imaging for the comparison of dynamics at different time points of postnatal development (Fig. 1-4 and 10) were set as 1 day. Developmental decline of spine turnover could be better illustrated with this imaging condition. Intervals of *in vivo* imaging for the comparison of wild-type and ASD mouse models at postnatal week 3 were set as 2 days (Fig. 6, 8, 9, 11-15). With longer time intervals, the rates of gain and loss of spines could be more reliably calculated, mainly because of the increased numbers of added/lost spines in a given pair of image stacks taken at two time points.

Whisker trimming

After first *in vivo* imaging session, all whiskers on the facial pad were trimmed with an electric razor (Fig. 4). As a control, we applied tactile stimuli equivalent to whisker trimming to the whiskers of control mice. To confirm the special relationship of the imaged area and the position of the barrel cortex (0.8 mm posterior from bregma and 3.2 mm lateral from midline), we injected rhodamine-dextran (1mg/ml, TMRD; Invitrogen, OR) into the imaged cortical area through the cranial window after *in vivo* imaging. After labeling of the imaged cortical area, we perfused the mice transcardially with 4% paraformaldehyde. Then, the fixed brains were removed and sectioned parallel to the surface of somatosensory cortex into 100 µm slice with a vibratome. The slices were examined under wide-field microscope for the relative positions of the dye injection sites and the barrel cortex, which could be detected by staining with anti-NeuN antibody (mouse monoclonal, A 60; Millipore, MA) followed by the fluorophore-conjugated secondary antibodies. Daily repetitive whisker trimming was conducted from PND 14 to PND 21. In PND 21, mice were perfused and sections of the barrel cortex were obtained. Dendrites in the barrel cortex were imaged with a laser scanning confocal microscopy (FV1000, Olympus), and the spine densities were measured.

Immunohistochemistry

Mice at postnatal week 3 were anesthetized and perfused with 4% paraformaldehyde. The brains were dissected and cut into 50 µm thick slices using a vibratome. Brain sections were treated with 0.5% Triton X-100 in PBS, blocked with 5% NGS, and then reacted with primary antibodies, followed by secondary antibodies. The antibodies used in this study were as follows: mouse anti-gephyrin (Synaptic Systems), guinea pig anti-VGluT2 (Millipore), rabbit anti-VGluT1[51], rabbit anti-Iba-1 (WAKO), Alexa 647-labeled goat anti-mouse IgG (Invitrogen), Alexa 647-labeled goat anti-guinea pig IgG (Invitrogen) and Alexa 488 or 647-labeled goat anti-rabbit IgG (Invitrogen). Images were obtained from layer 1 of the SSC using an FV1000 confocal laser-scanning microscope (Olympus) with a 60× oil-immersion lens (1.42 NA, PlanApoN, Olympus).

Data analysis

Image processing and analysis was performed using ImageJ software (NIH, http://rsb.info.nih.gov/ij). All analyses were performed using raw three dimensional stack images. The same dendritic segments were identified from the three dimensional stack images at different time points. We classified dendritic protrusions into either spines or filopodia. The filopodia were defined as long, thin structures without apparent spine heads and had not accumulated PSD-95-GFP. PSD-95-GFP-(−) spines had small spine heads and were shorter than typical filopodia. Furthermore, the survival rate of PSD-95-GFP-(−) spines over 1 day in 2-week-old mice was higher than that of filopodia [PSD-95-(−) spines, 50.0%; filopodia, 20.8%], indicating that PSD-95-GFP-(−) spines had properties different from those of filopodia. Spines were considered identical between the two images if they were within 0.5 µm of their expected positions, based on their spatial relationship to adjacent spines or other fiducial marks such as dendritic branch points. Newly-formed spines were those identified only at the second time point. Eliminated spines were those that existed only at the first time point but disappeared at the second time point. Spines present at both time points were categorized as stable spines. Because two-photon microscopy has lower resolution in the z-axis, only dendritic protrusions that were clearly projecting laterally were included in the analysis[52].

For the classification of spines with or without PSD-95-GFP clusters, we defined the clustering index (CI) as follows:

$$CI = (G_{spine}/R_{spine})/(G_{shaft}/R_{shaft}) \quad (1)$$

G_{spine} and R_{spine} were the average intensities of either PSD-95-GFP (G_{spine}) or DsRed2 (R_{spine}) fluorescence from boxed regions of interest (ROIs) (0.46 × 0.46 μm) positioned at the center of spine heads in a single plane of the z-stack images, where the intensity of the spine DsRed2 signal was highest and the spines were well separated from other fluorescent structures in the vicinity. ROIs were placed at the distal part of thin or stubby spines if they were without clear heads. G_{shaft} and R_{shaft} were the average intensities measured with an identical setting of ROIs but with their positions on nearby dendritic shafts. In some cases, G_{shaft} was not high enough for accurate measurement and was substituted by the average of multiple G_{shaft} values from the ROIs placed on dendrites with sufficient GFP signals and closest to the ROIs on spines. We sampled 1454 different dendritic positions for the calculation of G_{shaft}/R_{shaft} and found that 95% of individual G_{shaft}/R_{shaft} values were within 50%–200% of their average. Therefore, the threshold for the CI of PSD-95-GFP-(+) spines was set at 2.0 (Fig. 3b). Spines with their G_{spine}/R_{spine} values more than twice the G_{shaft}/R_{shaft} values were classified as spines containing PSD-95-GFP clusters.

For detection of gephyrin-GFP clusters, we first measured basal GFP intensities on the dendritic shafts (GFP_{shaft}) from 10 ROIs (0.46 × 0.46 μm) placed on the dendritic areas without gephyrin clusters. Pixels containing GFP fluorescence intensity more than two-fold of the GFP_{shaft} were isolated by thresholding, and binary images were created. Clustered pixels with their area more than 0.28 μm^2 in binary images were further isolated, and clusters with their average intensities more than twice the values of nearby dendritic regions were selected as gephyrin clusters. Gephyrin clusters were judged to be identical with criteria similar to the scoring of identical spines at different time points. Gephyrin-GFP-(+) spines were defined as the spines containing gephyrin-GFP clusters at the first or second imaging sessions. Gephyrin-GFP-(−) spines were the remaining spines without gephyrin-GFP clusters in both imaging sessions.

In this study we provided two types of parameters for the evaluation of spine dynamics. The first parameter was gain/loss of spines per unit length of dendrites. The second parameter was the turnover rate expressed as a percentage of newly formed and/or eliminated spines per total spines. To calculate these two types of parameters, we first measured the following values:

$L_{dendrite}$: length of dendritic segments analyzed

N_{total1} and N_{total2}: total number of spines in the first and second imaging sessions

N_{gain} and N_{loss}: number of appeared and disappeared spines between two imaging sessions

When spines were classified by either PSD-95-GFP or gephyrin-GFP, the above values were measured within each subset of classified spines. Using these values, the following parameters were calculated:

$$\text{Gain of spines per µm} = N_{gain}/L_{dendrite} \tag{2}$$

(Fig. 3d, 4a, 6b, 8d, h, 9g, 10d, 11d, h, 12b)

$$\text{Loss of spines per µm} = N_{loss}/L_{dendrite} \tag{3}$$

(Fig. 3d, 4a, 6b, 8d, h, 9g, 10d, 11d, h, 12b)

$$\text{Turnover rate (\%) of total spines} = (N_{gain} + N_{loss})/(N_{total1} + N_{total2}) \tag{4}$$

(Fig. 8c, g, 9f, 10c, 11c, g, 12a)

$$\text{Turnover rate (\%) of spine gain} = N_{gain}/((N_{total1} + N_{total2})/2) \tag{5}$$

(Fig. 1d, 2a, 14a)

$$\text{Turnover rate (\%) of spine loss} = N_{loss}/((N_{total1} + N_{total2})/2) \tag{6}$$

(Fig. 1d, 2a, 14a)

Gain and loss of gephyrin clusters in Figure 13b, c, e, and f were calculated using the formula similar to equations (2) and (3), with substitution of N_{gain} and N_{loss} by the number of appeared and disappeared gephyrin clusters between two imaging sessions, respectively.

To identify the transition between PSD-95-GFP-(+) and (−) spines, we calculated CIs of the individual spines at two time points using equation (1). Because we set the threshold of PSD-95-GFP clustering at CI as 2.0, new spines were categorized as PSD-positive if their CIs were higher than 2.0. Therefore, we defined the transition from PSD-negative to PSD-positive spines only when their CI changed to >2.0. The following equation defined the transition from PSD-negative to PSD-positive spines:

$$CI_{2nd} \geq CI_{1st} + 2.0 \quad \text{and} \quad CI_{1st} < 2.0 \qquad (7)$$

CI_{1st} and CI_{2nd} were CIs at the first and second imaging sessions. The transition from PSD-positive to PSD-negative spines was also defined by the following equation:

$$CI_{1st} \geq CI_{2nd} + 2.0 \quad \text{and} \quad CI_{2nd} < 2.0 \qquad (8)$$

The remaining spines were judged as PSD-negative when their CIs did not change to more than 2.0 and their average CIs were less than 2.0. These conditions can be described by the following equation:

$$| CI_{1st} - CI_{2nd} | < 2.0 \quad \text{and} \quad ((CI_{1st} + CI_{2nd})/2) < 2.0 \qquad (9)$$

The remaining spines were defined the PSD-positive spines at two time points. Spines with large spine heads (spines with large R_{spine}) may be erroneously categorized as PSD-95-negative spines. To evaluate this possibility, we randomly selected large persistent spines ($n = 30$) at postnatal week 8. Most of these stable spines in the mature cortex should have synaptic connections, and our protocol successfully categorized them as PSD-95-positive spines. By this protocol, CIs of all spines from two successive imaging sessions could be automatically classified into four types of dynamic spines and four types of persistent spines. Importantly, the manual classification of spines into the same categories by multiple investigators confirmed the validity of automatic categorization.

For measurement of spine volume, ROIs were set to cover the entire spine heads, and the integrated intensities of single spines in a single plane were quantified. Integrated intensities were normalized to the mean intensity of adjacent dendrites measured from boxed ROIs (0.75 × 0.75 μm). Backgrounds were subtracted before normalization.

For the analysis of apposition between dendritic spines and VGluT1, VGluT2 or gephyrin immunopositive puncta, we first selected dendritic spines from confocal images of DsRed2-filled dendrites. Subsequently, GFP images were overlaid with DsRed2 images that aided in judging the presence or absence of gephyrin-GFP or PSD-95-GFP clusters for each spine. Another investigator then manually analyzed the juxtapositon between dendritic spines and VGluT1, VGluT2 or gephyrin puncta in a blind manner without referring to the GFP images. When pixel areas corresponding to spine heads were contacted or overlapped with pixel areas judged positive with VGluT1, VGluT2 or gephyrin signals, the spines were scored to have apposition to VGluT1, VGluT2 or gephyrin puncta. To estimate the overlap at chance level, we prepared image stacks with a GFP channel shifted by 50 pixels (approximately 5 μm) in both x and y directions and performed the same analysis.

For statistical analysis, data are presented as means ± s.e.m. Paired means were compared using t-tests. Multiple means were compared using one-way ANOVA.

4. Results

Differential dynamics of spines classified by developmental stages and postsynaptic markers *in vivo*

The primary somatosensory barrel cortex (SSC) of rodents has been extensively studied as a model system of experience-dependent development of neural circuits[53,54]. In this analysis we first focused on synapses formed onto layer 2/3 pyramidal neurons in the SSC. These neurons are major integrators of sensory information and receive multiple inputs, including those from layer 4 spiny stellate cells, other layer 2/3 pyramidal cells, and the thalamus (thalamocortical axons: TCAs)[55]. Previous studies indicated a rapid postnatal increase of synapse density in the SSC[8,56,57], but precise developmental profiles of spines in layer 2/3 pyramidal neurons have not been obtained. Therefore, we measured the spine density of layer 2/3 pyramidal neurons expressed with PSD-95-GFP and DsRed2 along the course of postnatal development and found a rapid increase in spine density until postnatal week 3 and its stabilization thereafter (Fig. 1A and B).

To further illustrate the underlying mechanism of spine density increase, we next measured spine turnover *in vivo* (Fig. 1C and D). *In vivo* two-photon imaging revealed that the gain of spines exceeded loss at postnatal week 2, but it was downregulated and balanced with their loss at postnatal week 3. This timing was consistent with the developmental profile of total spine density (Fig. 1B and D), suggesting that the balance of gain and loss is an important determinant of the increase in postnatal spine density.

In this study we performed *in vivo* two-photon imaging mainly with a transcranial thinned-skull window[47,58], while in some experiments with young animals (Fig. 1-4 and 10), we applied the open-skull technique[48]. Importantly, the spine turnover rate at postnatal week 8 measured by using the open-skull window technique was 3.61% (Fig. 1D), which was in the range of spine turnover rates previously reported using the thinned-skull technique[59]. We further compared spine turnover rates with two types of cranial windows at postnatal week 3 and found no significant differences (Fig. 2A). Additionally we routinely checked the extent of glial activation after the open-skull surgery and found no sign of increase in Iba-1 immunoreactivity, indicating little activation of microglia (Fig. 2B and C). From these considerations, we concluded that the dynamic properties measured through the open-skull windows reliably report the turnover of native synapses *in vivo*.

We utilized two types of markers, PSD-95 tagged with GFP (PSD-95-GFP) and gephyrin tagged with GFP (gephyrin-GFP), for classification of spines imaged *in vivo*.

PSD-95-GFP clusters are a reliable marker for the postsynaptic structure[10,43,60]. Therefore, spines containing PSD-95-GFP [PSD-95-GFP-(+) spines] can be classified as more differentiated spines. We observed apical dendrite expressing DsRed2 and PSD-95-GFP (Fig. 3A), and the accumulation of PSD-95-GFP to spine was defined by CI score (refer to materials and methods). Because 95% of individual Gshaft/Rshaft values were within 50%-200% of their average (Fig. 3B), we set the threshold for the CI of PSD-95-GFP-(+) spines at 2.0. Consistent with this idea, PSD-95-GFP-(−) spines were a minor fraction compared with PSD-95-GFP-(+) spines and their volumes were significantly smaller (Fig. 3C). PSD-95-GFP-(−) spines were distinct from dendritic filopodia based on their differences in lifetimes, because the survival rate of PSD-95-GFP-(−) spines over 1 day in 2-week-old mice was higher than that of filopodia [PSD-95-(−) spines, 50.0%; filopodia, 20.8%]. The grouping of spines with or without PSD-95-GFP clusters along postnatal development revealed selective increases of PSD-95-GFP-(+) spines from PND 7 to 22, without significant changes in the density of PSD-95-GFP-(−) spines (Fig. 1B).

In vivo time-lapse imaging over 1 day at postnatal weeks 2, 3, and 8 revealed important properties of PSD-95-GFP-(+) spines (Fig. 3A and D). First, the dynamics of PSD-95-GFP-(+) spines were developmentally downregulated. Because the fractions of spines without PSD-95 clusters were small, the suppression of PSD-95-GFP-(+) spine dynamics underlies the downregulation of total spine turnover. Second, acquisition of PSD-95-GFP clusters within pre-existing PSD-95-GFP-(−) spines cannot explain the appearance of PSD-95-GFP-(+) spines. Within 24 h, the number of newly formed PSD-95-GFP-(+) spines was 2.36 ± 0.14 per 100 μm of dendrites at postnatal week 3 (Fig. 3D). However, the transition events from PSD-95-GFP-(−) to (+) spines were less frequent (0.73 ± 0.08 per 100 μm of dendrites; 12 events per 655 spines, n = 4 animals), indicating that a large fraction of PSD-95-GFP-(+) spines were generated de novo within 24 h. Furthermore, the rate of net increase in PSD-95-GFP (+) spines estimated by *in vivo* imaging at postnatal 2 weeks (lines in Fig. 3E) matched the actual speed of spine synapse increase (data points in Fig. 3E). These results indicate that the developmental profile of spine synapse density in the early postnatal period is regulated by the balance between gain and loss of PSD-95 (+) spines. Taken together with the developmental profiles of PSD-95-GFP-(+) spine increase (Fig. 1B), we concluded that a turnover of PSD-95-GFP-(+) spines and its developmental regulation mainly contribute to the formation of stable neural circuits in the mature neocortex.

Was rapid formation of postsynaptic spines regulated by activity? To address this question, we next performed *in vivo* time-lapse imaging through open-SSC windows at postnatal 2 weeks with manipulation of sensory stimuli by trimming all whiskers on the facial pad[25]. This manipulation suppressed turnover of PSD-95-GFP (+) spines through selective reduction in the de novo formation of PSD-95-GFP (+) spines, without affecting their elimination rate (Fig.4). Daily whisker trimming from PND14 to PND21 caused reduction of the total density of PSD-95-GFP (+) spines, without changing the density of PSD-95-GFP (-) spines (Fig. 4B). These analyses indicate that increase of synapse density is regulated by sensory stimuli through the rapid generation of new dendritic protrusions with postsynaptic specialization.

The second marker we utilized for spine classification is gephyrin-GFP (Fig. 5A). Layer 2/3 pyramidal neurons receive excitatory afferents from multiple neuronal populations. A subset of spines receives inhibitory inputs from local interneurons, and these spines also form excitatory synaptic connections with TCAs[15]. Therefore, the identification of spines containing gephyrin-GFP may be useful in the grouping of heterogeneous spine populations. A majority of gephyrin-GFP-(+) spines (64%) was apposed to puncta immunoreactive with VGluT2, a reliable marker of presynaptic terminals of TCAs (Fig. 5B and C). In contrast, the association of gephyrin-GFP-(+) spines with VGluT1, a marker of intracortical axon terminals, was at chance level (28% versus 25 % for image-shifted controls). Conversely, we confirmed the preferential apposition of gephyrin-GFP-(−) spines to VGluT1-positive terminals [64% of gephyrin-GFP-(−) spines], while apposition of gephyrin-GFP-(−) spines to VGluT2-positive terminals was at chance level (25% versus 29% for image-shifted controls) (Fig. 5B and C). A majority of spines apposed to puncta immunoreactive with gephyrin (95%) contained PSD-95-GFP (Fig. 5D and E). Furthermore, gephyrin-GFP-(+) spines were 20% of the total spines and larger than gephyrin-GFP-(−) spines (Fig. 5F and G), further supporting their distinct properties. Our quantitative analysis of spine volume suggests little overlap between PSD-95-GFP-(−) and gephyrin-GFP-(+) spines (Fig. 3C and 5G). These data indicated that gephyrin-GFP-(+) spines were a subset of PSD-95-GFP-(+) spines.

We next examined the dynamics of gephyrin-GFP-(+) and (−) spines by *in vivo* imaging of mice at postnatal week 3. *In vivo* time-lapse imaging over 2 days at postnatal week 3 revealed distinct dynamic properties of gephyrin-GFP-(+) and (−) spines (Fig. 6A). Gephyrin-GFP-(+) spines were extremely stable compared with gephyrin-GFP-(−) spines (Fig. 6B). Because the turnover rates of gephyrin-GFP-(+) spines were lower than those of total spines at postnatal week 8 (Fig. 3D and 6B), the differences in the extent of differentiation cannot explain the stability of the gephyrin-GFP-(+) spines. From these observations, we concluded that the turnover of gephyrin-GFP-(+) and (−)

spines reflects distinct dynamic properties of thalamocortical synapses and intracortical synapses onto the same postsynaptic dendrites of layer 2/3 neurons.

Enhanced turnover of specific spine subtypes in patDp/+ mice

The *in vivo* visualization technique of spines marked by either excitatory or inhibitory postsynaptic scaffolds was applied to the detection of synaptic phenotypes in ASD mouse models. We first analyzed a mouse model of nonsyndromic ASD, in which the chromosomal region corresponding to human 15q11–13 is paternally duplicated (patDp/+ mice)[39]. By setting a specific time window at postnatal week 3 in the initial analysis of the ASD mouse model afterward, we aimed to detect any impairment in the regulatory mechanisms of spine remodeling. In this time window, spine density already reached the level of mature SSC, but active remodeling of spines still occurs and both functional and structural plasticity is robust[47,53,58]. There were no apparent abnormalities in the architecture of SSC (Fig. 7A and B) and the density of spines (Fig. 8A and B) in patDp/+ mice. We performed *in vivo* imaging and measured the turnover of spines marked by PSD-95-GFP in the SSC of wild-type and patDp/+ mice over 2 days at postnatal week 3 (Fig, 8A). We found that the turnover of PSD-95-GFP-(+) spines were significantly enhanced (Fig. 8C) and the gain and loss of PSD-95-GFP-(+) spines increased in patDp/+ mice (Fig. 8D). However, the dynamics of PSD-95-GFP-(−) spines were comparable between patDp/+ and wild-type mice (Fig. 8C and D). These results indicated that genetic modifications mimicking the duplication of human chromosome 15q11–13 preferentially affected the remodeling of PSD-95-GFP-(+) spines, which contributed to the establishment of stable neural circuits in the SSC.

We next performed *in vivo* imaging of spines marked by gephyrin-GFP in wild-type and patDp/+ mice (Fig. 8E). No significant differences were present in the fraction of spines positive with gephyrin-GFP between patDp/+ and wild-type mice (Fig. 8F). Our *in vivo* imaging over 2 days revealed that the dynamics of gephyrin-GFP-(−) spines were significantly enhanced in patDp/+ mice, whereas the stability of gephyrin-GFP-(+) spines were comparable between patDp/+ and wild-type mice (Fig. 8G and H). This indicates that genetic modifications mimicking the duplication of human chromosome 15q11–13 specifically affected the remodeling of gephyrin-GFP-(−) spines, which mainly receive inputs from other cortical neurons. Because patDp/+ mice showed enhanced turnover in PSD-95-GFP-(+) and gephyrin-GFP-(−) spines, we concluded that a specific subset of spines differentiating excitatory synaptic contacts with intracortical afferents show enhanced turnover in patDp/+ mice.

Abnormal synaptic dynamics in multiple cortical areas and at different developmental stages in patDp/+ mice

We detected an enhanced turnover of PSD-95-GFP-(+) spines as a major synaptic phenotype in the SSC of patDp/+ mice. We aimed to determine whether the synaptic phenotypes observed in the SSC at postnatal week 3 could be generalized to different cortical areas and developmental stages. Several lines of evidence indicated that the rodent anterior frontal cortex (AFC) may be defective in ASD mouse models. First, studies in patients with ASD indicated dysfunction and early postnatal overgrowth in the frontal cortex[61]. Second, pyramidal neurons in the AFC showed hyperconnectivity in an ASD mouse model[62]. Third, from PND 2 to 21, the AFC receives a large number of long-distance intracortical projections[63], which are considered to be less developed in patients with ASD[61]. The AFC imaged in this study was anterior to the primary motor cortex[64] and distinct from the rodent prefrontal cortex[65] (Fig. 9 A, B and C). The architecture of AFC (Fig. 7C and D) and the density of spines (Fig. 9D and E) in the AFC were not different between wild-type and patDp/+ mice. We found that the dynamics of PSD-95-GFP-(+) spines was enhanced in the AFC of patDp/+ mice (Fig. 9F) and both the gain and loss of PSD-95-GFP (+) spines increased (Fig. 9G). Upregulation of spine turnover was comparable between the AFC and SSC, indicating the presence of autism-related synaptic phenotypes in multiple cortical areas (compare Fig. 8C and 9F).

We next performed *in vivo* imaging of patDp/+ mice over 1 day at postnatal week 2 (Fig. 10A and B). We found that the gain and loss of PSD-95-GFP-(+) spines were also upregulated in patDp/+ mice at postnatal week 2 (Fig. 10C and D). In wild-type mice, the gain of PSD-95-GFP-(+) spines exceeded their loss at this time point (Fig. 10D), and this relationship was reversed at postnatal week 3 (Fig. 8D). This shift in the balance between spine gain and loss was preserved in patDp/+ mice (Fig. 8D and 10D). The rates of gain and loss of PSD-95-GFP-(−) spines were also enhanced at postnatal week 2 (Fig. 10D), suggesting the presence of a developmental stage-specific phenotype in patDp/+ mice. In summary, enhanced turnover of PSD-95-GFP-(+) spines is likely to be a common phenotype across different cortical areas and developmental stages.

Shared spine phenotypes in patDp/+ and NLG R451C mice

If multiple mouse models of nonsyndromic ASDs share similar defects in synapse remodeling, this information in similarity should be useful in defining the core characteristics of ASDs. To test if the enhanced turnover of synapses was present in other mouse models, we next analyzed NLG R451C mice[29], which are engineered to have a rare missense mutation of neuroligin-3 found in nonsyndromic ASDs. We first evaluated the spine density and dynamics of PSD-95-GFP-(+) spines in the AFC at postnatal week 3 (Fig. 11A). Although the architecture of AFC (Fig. 7C and D) and the density of spines were not altered in the AFC of NLG R451C mice (Fig. 11B), *in vivo* imaging of NLG R451C mice showed enhanced dynamics of PSD-95-GFP-(+) spines (Fig. 11C and D). Upregulation of spine turnover was comparable between NLG R451C and patDp/+ mice, indicating the presence of the autism-related common synaptic phenotype in the AFC of multiple mouse models. The gain and loss of PSD-95-GFP-(+) spines significantly increased in the AFC of NLG R451C mice (Fig. 11D).

To further evaluate the similarities of synaptic dynamics in multiple ASD mouse models, we next tested if spines classified by the presence of gephyrin-GFP clusters in the SSC show similar defects in NLG R451C mice (Fig. 11E). The architecture of SSC (Fig. 7A and B) and the densities of gephyrin-GFP-(+) and (−) spines in the SSC were comparable between NLG R451C and wild-type mice (Fig. 11F). Similar to patDp/+ mice, *in vivo* imaging showed that the turnover of gephyrin-GFP-(−) spines was enhanced in NLG R451C mice, whereas gephyrin-GFP-(+) spines were highly stable and their dynamics were comparable between wild-type and NLG R451C mice (Fig. 11G and H).

Our *in vivo* imaging experiments using two mouse models of nonsyndromic ASDs revealed remarkably similar alterations in the dynamics of specific spine subsets. We further extended *in vivo* imaging analyses of PSD-95-GFP-(+) spines to the third ASD mouse model, BTBR mice[42]. Dynamics of PSD-95-GFP-(+) spines in the AFC of BTBR mice at postnatal week 3 were once more upregulated to a similar extent (Fig. 12). We concluded that the enhanced turnover of PSD-95-GFP-(+) spines that participated in the intracortical connectivity underlay autism-related deficits in the cortex of multiple ASD mouse models.

Specific alterations of inhibitory synaptic dynamics in patDp/+ mice

To investigate if the turnover of inhibitory synapses per se is altered in ASD mouse models, we measured the number of newly added and lost gephyrin clusters in patDp/+ and NLG R451C mice. One-third of gephyrin-GFP clusters were localized within spines and the remaining two-thirds were on dendritic shafts (Fig. 5F). The densities of shaft gephyrin clusters in patDp/+ and NLG R451C mice were comparable with wild-type mice (Fig. 13A and D). *In vivo* imaging of the SSC over 2 days at postnatal week 3 revealed enhanced dynamics of shaft gephyrin clusters in patDp/+ mice (Fig. 13B), whereas NLG R451C mice showed dynamics of shaft gephyrin clusters comparable with wild-type mice (Fig. 13E). The turnover of spine gephyrin clusters was not altered in both ASD mouse models (Fig. 13C and F). The observed changes in the shaft gephyrin clusters may be related to specific impairments of neuronal functions present in patDp/+ mice.

Relative distances between spines and inhibitory synapses may influence the stability of spines. Shaft gephyrin clusters were more stable than spine gephyrin clusters, and the fluorescence intensities of shaft clusters were higher than those of the spine clusters (Fig. 14). Therefore, we focused on shaft gephyrin clusters and tested if the presence of shaft gephyrin clusters affects the stability of nearby spines. We found that spines within 4 µm of shaft gephyrin clusters were less stable than those more than 4 µm away from shaft gephyrin clusters (Fig. 15). Furthermore, this effect of nearby gephyrin clusters on spine stability was abolished in both patDp/+ and NLG R451C mice. These results indicated that both the dynamics of inhibitory synapses and the influence of inhibitory shaft synapses on nearby spines can be affected by genetic mutations related to ASDs.

5. Discussion

In this study, we measured the dynamics of excitatory synapses by visualizing spines and PSDs in the early postnatal cortex. The results obtained from these experiments revealed that the balance between gain and loss of spines containing PSD mostly contributed to the increase of spine and PSD density. A previous study reported that synapses labeled by PSD-95-GFP in live zebrafish larvae were actively generated and eliminated. This study showed that synapse formation plays an essential role in stabilizing the dendrite on which it is located[66]. Gray and his colleagues first reported spine dynamics of PSD-95 in mice[60], but their quantitative data of spine turnover did not include classifications by PSD-95 clusters. Our study provides more accurate quantitative measurements, because the results were obtained from dendrites after termination of dendritic growth and based on PSD-95 as a marker of synapses.

How is the balance between gain and loss of synapses, which play a critical role in increasing synapse number, regulated? Previous studies in a developmental stage earlier than postnatal 2 weeks indicated that spines and initial neural circuits are formed independently of activity[67,68], and then silent synapses containing only NMDA receptors switch to functional synapses in an activity-dependent manner[69]. In this study, we have shown that de novo formation of PSD-95-(+) spines requires sensory inputs at postnatal

2 weeks, suggesting that the mechanism of spine formation changes from an activity-independent to an activity-dependent manner during the process of development. On the other hand, these active remodeling of synapses are suppressed after postnatal 3 weeks. We could not reveal the mechanism regulating the change in synapse dynamics associated with development. A recent study exhibited that the suppression of spine dynamics no longer occurred in Nogo receptor knock-out adult mice, originally identified as a mediator of myelin-dependent restriction of recovery from injury[70], and suggested that Nogo signaling might regulate developmental synaptic dynamics. Alternatively, the sensory cortex has different critical periods depending on each modality[71]. Since many studies have examined the molecular mechanisms of onset and end of critical periods, we will be able to further clarify the mechanism regulating synapse dynamics by observing neurons modulated by molecular expression or signals related to critical periods.

During development, neural circuits are established with extensive remodeling of synapses. Our imaging study using multiple ASD mouse models suggests that an enhanced turnover of excitatory synapses is a common phenotype of nonsyndromic ASD mouse models. In addition, detailed analyses of spine subtypes using an inhibitory postsynaptic marker, gephyrin, revealed that a subset of spines associated with afferents from cortical neurons exhibited enhanced turnover. These results suggest that abnormal dynamics of a specific population of synapses during development underlies cortical dysfunctions in ASDs.

We found an enhanced turnover of spines in ASD mouse models with distinct genetic backgrounds. In patDp/+ mice, genes such as *Ndn*, *Snrpn, Gabrα5, Gabrβ3*, *Gabrγ3* and snoRNA are upregulated[39]. Altered RNA editing and calcium influx through 5-HT2c receptors by abnormal snoRNA expression were proposed to be a candidate mechanism related to autism in patDp/+[39]. NLG R451C mice display an enhancement of mIPSC frequency and increased expression of inhibitory synapse-related proteins[29]. Because neuroligin-3 is localized to both excitatory and inhibitory synapses[72], the enhancement of spine dynamics may result from abnormal function of neuroligin-3 in excitatory synapses. BTBR mice, the inbred strain identified by behavioral screening to mimic the core behavioral deficits of ASD, also showed a similar enhanced spine turnover. In addition to the ASD mouse models that were analyzed in this study, the *Fmr1* KO mice, a fragile X syndrome and syndromic autistic mouse model, displayed enhanced spine turnover[4,73], further supporting the idea that an increase in synapse turnover is a common phenotype across diverse ASD mouse models.

How do diverse genetic mutations in these ASD mouse models lead to a highly similar phenotype in the turnover of excitatory synapses? Synapse turnover is regulated by both activity-dependent and -independent pathways[10,47,74]. Synapses can still be generated without activity, but the process of synapse stabilization may be selectively affected by activity[75]. If diverse genetic mutations in these mouse models converge to impair activity-dependent stabilization, mice models may show similar enhancement in synapse turnover. An obvious candidate pathway is N-methyl-D-aspartate (NMDA) receptor-dependent signaling[76], and a previous study indicated defects in NMDA receptor-dependent synaptic plasticity in ASD mouse models, including NLG R451C mice[77].

In this study, we found that enhanced spine turnover was restricted to gephyrin-GFP-(−) spines receiving intracortical projections in the SSC at postnatal week 3. The enhancement of gephyrin-GFP-(−) spines was observed in both patDp/+ and NLG R451C mice. Thus, this selective impairment may be a common property of ASD mouse models. Gephyrin-GFP-(+) and (−) spines were present within the same dendritic segments but their dynamic properties were distinct. Large gephyrin-GFP-(+) spines were highly stable and unaffected by ASD-related gene mutations, while smaller gephyrin-GFP-(−) spines were more dynamic and vulnerable to genetic manipulations mimicking ASDs. If the spine phenotypes identified in ASD mouse models were due to nonspecific deteriorative effects on postsynaptic pyramidal neurons, both types of spines should have been affected. Selective alterations in gephyrin-GFP-(−) spines suggest important roles of presynaptic partners in the expression of ASD-related phenotypes.

Vulnerability of specific spine subtypes may be explained by the different onset and closure of experience-dependent plasticity in two types of synaptic connections. Previous developmental studies of layer 4-layer 2/3 synapses indicated that synaptic plasticity begins and is most robust on PND12−14 but is present even in adulthood[53,78]. In the case of synapses between TCAs and layer 4 neurons, synaptic plasticity has been reported to occur only up to PND 7[13]. If synapses between TCAs and layer 2/3 neurons have a time window of plasticity similar to those of layer 4 neurons, the difference in spine remodeling between those receiving intracortical projections and TCAs may be explained by the early closure of plasticity in TCAs-layer 2/3 synapses. One can also argue that TCAs-layer 2/3 synapses may have distinct properties. Layer 4 stellate cells and layer 2/3 pyramidal cells are projected from different regions of the thalamus (ventral posteromedial nucleus to layer 4 neurons and medial posterior nucleus to layer 2/3 neurons)[79], and these projections transmit signals that have originated from distinct peripheral regions (lemniscal inputs through the ventral posteromedial nucleus and paralemniscal inputs through the medial posterior nucleus)[80]. It is possible that TCAs-layer 2/3 synapses, which transmit global and multisensory information to the SSC, are less influenced by activity-dependent mechanisms of synapse remodeling. This may explain why TCAs-layer 2/3 synapses are highly stable and less influenced by ASD-related genetic mutations.

Identification of both common and distinct synaptic phenotypes from multiple ASD mouse models may further extend our understanding of the pathophysiology of ASD. In this study, we detected an enhanced turnover of shaft gephyrin clusters in patDp/+ mice but not in NLG R451C mice. The imbalance between excitatory and inhibitory synaptic inputs has been proposed to contribute to the pathophysiology of ASD[23,81]. NLG R451C mice show an increase in spontaneous inhibitory synaptic events[29]. Conditional knockout of *Mecp2* in inhibitory neurons induced a reduction in inhibitory signaling and autism-like stereotypes[27]. Mice with mutant *Scn1a* gene, which is responsible for Dravet’s syndrome, show autistic-like behavior and impairment in GABAergic transmission[30]. These studies indicate that both upregulation and suppression of inhibitory synaptic transmission are associated with autistic-like behavior in model mice. Activity of interneurons should be regulated by multiple factors, including the average level of local circuit activity, feed-forward and feedback mechanisms of information processing, synchronization and oscillation of neuronal populations, and neuromodulatory signals. The level of inhibitory synaptic transmission is likely regulated by the integration of multiple factors altered in the cortex of ASD mouse models. Further characterization of neuronal connectivity via inhibitory synapses in the process of early cortical development may provide more information on the role of inhibitory synapses in the pathophysiology of ASD.

In addition to alterations in synapse remodeling, we found disruption in the effect of shaft gephyrin clusters on the stability of nearby spines in ASD mouse models. *In vivo* imaging of both dendritic spines and gephyrin clusters indicated that remodeling of spines and inhibitory shaft synapses is spatially clustered and monocular deprivation increased the frequency of clustering events[82]. These results indicate that the spatial relationship between synapses plays an important role in experience-dependent remodeling of cortical neuron connectivity. The negative effects of shaft inhibitory synapses on nearby spines may be important in the regulation of a clustered formation of spines. Clustering of new spines and inhibitory shaft synapses in the visual cortex may be explained by assuming that the positions of shaft inhibitory synapses determine the hot spots of synapse remodeling, where both new spines and new inhibitory synapses are more likely to be formed. Inhibitory current suppresses the propagation and the integration of depolarizing current generated from excitatory synapses. Disruption of local interactions between shaft inhibitory synapses and nearby spines in ASD mouse models may have important consequences in local dendritic integration of synaptic inputs[83]. A recent analysis of ensemble activity in the SSC of *Fmr1* KO mice indicated an abnormally high synchrony of network activity[84]. Further physiological investigations to test if an imbalance in local excitatory/inhibitory inputs underlies circuit level deficits in ASD mouse models may provide useful insight into the mechanism of onset and progress of ASD.

6. References

1. Okabe, S. Fluorescence imaging of synapse formation and remodeling. *Microscopy* **62,** 51–62 (2013).

2. Jontes, J. D., Buchanan, J. & Smith, S. J. Growth cone and dendrite dynamics in zebrafish embryos: early events in synaptogenesis imaged in vivo. *Nat. Neurosci.* **3,** 231–7 (2000).

3. Holtmaat, A. & Svoboda, K. Experience-dependent structural synaptic plasticity in the mammalian brain. *Nat. Rev. Neurosci.* **10,** 647–58 (2009).

4. Pan, F., Aldridge, G. M., Greenough, W. T. & Gan, W.-B. Dendritic spine instability and insensitivity to modulation by sensory experience in a mouse model of fragile X syndrome. *Proc. Natl. Acad. Sci. U. S. A.* **107,** 17768–73 (2010).

5. Grutzendler, J., Kasthuri, N. & Gan, W.-B. Long-term dendritic spine stability in the adult cortex. *Nature* **420,** 812–6 (2002).

6. Trachtenberg, J. *et al.* Long-term in vivo imaging of experience-dependent synaptic plasticity in adult cortex. *Nature* **420,** 788–94 (2002).

7. Yang, G., Pan, F. & Gan, W.-B. Stably maintained dendritic spines are associated with lifelong memories. *Nature* **462,** 920–4 (2009).

8. Miller, M. Maturation of rat visual cortex. I. A quantitative study of Golgi-impregnated pyramidal neurons. *J. Neurocytol.* **10,** 859–78 (1981).

9. Nägerl, U. V., Köstinger, G., Anderson, J. C., Martin, K. A. C. & Bonhoeffer, T. Protracted synaptogenesis after activity-dependent spinogenesis in hippocampal neurons. *J. Neurosci.* **27,** 8149–56 (2007).

10. Okabe, S., Kim, H. D., Miwa, A., Kuriu, T. & Okado, H. Continual remodeling of postsynaptic density and its regulation by synaptic activity. *Nat. Neurosci.* **2,** 804–11 (1999).

11. Petersen, C. C. H. The functional organization of the barrel cortex. *Neuron* **56,** 339–55 (2007).

12. Meyer, H. S. *et al.* Cell type-specific thalamic innervation in a column of rat vibrissal cortex. *Cereb. Cortex* **20,** 2287–303 (2010).

13. Crair, M. C. & Malenka, R. C. A critical period for long-term potentiation at thalamocortical synapses. *Nature* **375,** 325–8 (1995).

14. Ohno, S. *et al.* A Morphological Analysis of Thalamocortical Axon Fibers of Rat Posterior Thalamic Nuclei: A Single Neuron Tracing Study with Viral Vectors. *Cereb. Cortex* **22,** 2840–57 (2012).

15. Kubota, Y., Hatada, S., Kondo, S., Karube, F. & Kawaguchi, Y. Neocortical inhibitory terminals innervate dendritic spines targeted by thalamocortical afferents. *J. Neurosci.* **27,** 1139–50 (2007).

16. Geschwind, D. H. Advances in autism. *Annu. Rev. Med.* **60,** 367–80 (2009).

17. Amaral, D. G., Schumann, C. M. & Nordahl, C. W. Neuroanatomy of autism. *Trends Neurosci.* **31,** 137–45 (2008).

18. Courchesne, E. & Pierce, K. Why the frontal cortex in autism might be talking only to itself: local over-connectivity but long-distance disconnection. *Curr. Opin. Neurobiol.* **15,** 225–30 (2005).

19. Penzes, P., Cahill, M. E., Jones, K. A., VanLeeuwen, J.-E. & Woolfrey, K. M. Dendritic spine pathology in neuropsychiatric disorders. *Nat. Neurosci.* **14,** 285–93 (2011).

20. Zoghbi, H. Y. Postnatal neurodevelopmental disorders: meeting at the synapse? *Science* **302,** 826–30 (2003).

21. Geschwind, D. H. Autism: many genes, common pathways? *Cell* **135,** 391–5 (2008).

22. State, M. W. & Levitt, P. The conundrums of understanding genetic risks for autism spectrum disorders. *Nat. Neurosci.* **14,** 1499–506 (2011).

23. Südhof, T. C. Neuroligins and neurexins link synaptic function to cognitive disease. *Nature* **455,** 903–11 (2008).

24. Auerbach, B., Osterweil, E. & Bear, M. Mutations causing syndromic autism define an axis of synaptic pathophysiology. *Nature* **480,** 63–8 (2011).

25. Bangash, M. A. *et al.* Enhanced polyubiquitination of Shank3 and NMDA receptor in a mouse model of autism. *Cell* **145,** 758–72 (2011).

26. Baudouin, S. J. *et al.* Shared synaptic pathophysiology in syndromic and nonsyndromic rodent models of autism. *Science* **338,** 128–32 (2012).

27. Chao, H.-T. *et al.* Dysfunction in GABA signalling mediates autism-like stereotypies and Rett syndrome phenotypes. *Nature* **468,** 263–9 (2010).

28. Peça, J. *et al.* Shank3 mutant mice display autistic-like behaviours and striatal dysfunction. *Nature* **472,** 437–42 (2011).

29. Tabuchi, K. *et al.* A neuroligin-3 mutation implicated in autism increases inhibitory synaptic transmission in mice. *Science* **318,** 71–6 (2007).

30. Han, S. *et al.* Autistic-like behaviour in Scn1a+/- mice and rescue by enhanced GABA-mediated neurotransmission. *Nature* **489,** 385–90 (2012).

31. Chen, R. Z., Akbarian, S., Tudor, M. & Jaenisch, R. Deficiency of methyl-CpG binding protein-2 in CNS neurons results in a Rett-like phenotype in mice. *Nat. Genet.* **27,** 327–31 (2001).

32. Goorden, S. M. I., van Woerden, G. M., van der Weerd, L., Cheadle, J. P. & Elgersma, Y. Cognitive deficits in Tsc1+/- mice in the absence of cerebral lesions and seizures. *Ann. Neurol.* **62,** 648–55 (2007).

33. Guy, J., Hendrich, B., Holmes, M., Martin, J. E. & Bird, A. A mouse Mecp2-null mutation causes neurological symptoms that mimic Rett syndrome. *Nat. Genet.* **27,** 322–6 (2001).

34. Mineur, Y. S., Huynh, L. X. & Crusio, W. E. Social behavior deficits in the Fmr1 mutant mouse. *Behav. Brain Res.* **168,** 172–5 (2006).

35. Lang, M. *et al.* Selective preservation of MeCP2 in catecholaminergic cells is sufficient to improve the behavioral phenotype of male and female Mecp2-deficient mice. *Hum. Mol. Genet.* **22,** 358–71 (2013).

36. Michalon, A. *et al.* Chronic pharmacological mGlu5 inhibition corrects fragile X in adult mice. *Neuron* **74,** 49–56 (2012).

37. Sato, A. *et al.* Rapamycin reverses impaired social interaction in mouse models of tuberous sclerosis complex. *Nat. Commun.* **3,** 1292 (2012).

38. Abrahams, B. S. & Geschwind, D. H. Advances in autism genetics: on the threshold of a new neurobiology. *Nat. Rev. Genet.* **9,** 341–55 (2008).

39. Nakatani, J. *et al.* Abnormal behavior in a chromosome-engineered mouse model for human 15q11-13 duplication seen in autism. *Cell* **137,** 1235–46 (2009).

40. Silver, L. M. Mouse t haplotypes. *Annu. Rev. Genet.* **19,** 179–208 (1985).

41. Ellis, H. T., Tordoff, M. G. & Parker, M. R. Itpr3 Is responsible for the mouse tufted (tf) locus. *J. Hered.* **104,** 295–7 (2013).

42. McFarlane, H. G. *et al.* Autism-like behavioral phenotypes in BTBR T+tf/J mice. *Genes. Brain. Behav.* **7,** 152–63 (2008).

43. Okabe, S., Miwa, A. & Okado, H. Spine formation and correlated assembly of presynaptic and postsynaptic molecules. *J. Neurosci.* **21,** 6105–14 (2001).

44. Kuriu, T., Yanagawa, Y. & Konishi, S. Activity-dependent coordinated mobility of hippocampal inhibitory synapses visualized with presynaptic and postsynaptic tagged-molecular markers. *Mol. Cell. Neurosci.* **49,** 184–95 (2012).

45. Niwa, M. *et al.* Knockdown of DISC1 by in utero gene transfer disturbs postnatal dopaminergic maturation in the frontal cortex and leads to adult behavioral deficits. *Neuron* **65,** 480–9 (2010).

46. Tabata, H. & Nakajima, K. Efficient in utero gene transfer system to the developing mouse brain using electroporation: visualization of neuronal migration in the developing cortex. *Neuroscience* **103,** 865–72 (2001).

47. Zuo, Y., Yang, G., Kwon, E. & Gan, W.-B. Long-term sensory deprivation prevents dendritic spine loss in primary somatosensory cortex. *Nature* **436,** 261–5 (2005).

48. Holtmaat, A. *et al.* Long-term, high-resolution imaging in the mouse neocortex through a chronic cranial window. *Nat. Protoc.* **4,** 1128–44 (2009).

49. Yang, G., Pan, F., Parkhurst, C. N., Grutzendler, J. & Gan, W.-B. Thinned-skull cranial window technique for long-term imaging of the cortex in live mice. *Nat. Protoc.* **5,** 201–8 (2010).

50. Isshiki, M. & Okabe, S. Evaluation of cranial window types for in vivo two-photon imaging of brain microstructures. *Microscopy* (2013). in press doi:10.1093/jmicro/dft043

51. Takamori, S., Rhee, J. S., Rosenmund, C. & Jahn, R. Identification of a vesicular glutamate transporter that defines a glutamatergic phenotype in neurons. *Nature* **407,** 189–94 (2000).

52. Kondo, S., Kohsaka, S. & Okabe, S. Long-term changes of spine dynamics and microglia after transient peripheral immune response triggered by LPS in vivo. *Mol. Brain* **4,** 27 (2011).

53. Fox, K. Anatomical pathways and molecular mechanisms for plasticity in the barrel cortex. *Neuroscience* **111,** 799–814 (2002).

54. Feldman, D. E. & Brecht, M. Map plasticity in somatosensory cortex. *Science* **310,** 810–5 (2005).

55. *The Synaptic Organization of the Brain*. 736 (Oxford University Press, USA, 2003). at

56. De Felipe, J., Marco, P., Fairén, a & Jones, E. G. Inhibitory synaptogenesis in mouse somatosensory cortex. *Cereb. Cortex* **7,** 619–34 (1997).

57. Ashby, M. C. & Isaac, J. T. R. Maturation of a recurrent excitatory neocortical circuit by experience-dependent unsilencing of newly formed dendritic spines. *Neuron* **70,** 510–21 (2011).

58. Zuo, Y., Lin, A., Chang, P. & Gan, W.-B. Development of long-term dendritic spine stability in diverse regions of cerebral cortex. *Neuron* **46,** 181–9 (2005).

59. Xu, H.-T., Pan, F., Yang, G. & Gan, W.-B. Choice of cranial window type for in vivo imaging affects dendritic spine turnover in the cortex. *Nat. Neurosci.* **10,** 549–51 (2007).

60. Gray, N. W., Weimer, R. M., Bureau, I. & Svoboda, K. Rapid redistribution of synaptic PSD-95 in the neocortex in vivo. *PLoS Biol.* **4,** e370 (2006).

61. Courchesne, E. *et al.* Mapping Early Brain Development in Autism. *Neuron* **56,** 399–413 (2007).

62. Qiu, S., Anderson, C. T., Levitt, P. & Shepherd, G. M. G. Circuit-specific intracortical hyperconnectivity in mice with deletion of the autism-associated Met receptor tyrosine kinase. *J. Neurosci.* **31,** 5855–64 (2011).

63. Mitchell, B. D. & Macklis, J. D. Large-scale maintenance of dual projections by callosal and frontal cortical projection neurons in adult mice. *J. Comp. Neurol.* **482,** 17–32 (2005).

64. Tennant, K. A. *et al.* The organization of the forelimb representation of the C57BL/6 mouse motor cortex as defined by intracortical microstimulation and cytoarchitecture. *Cereb. Cortex* **21,** 865–76 (2011).

65. Van De Werd, H. J. J. M., Rajkowska, G., Evers, P. & Uylings, H. B. M. Cytoarchitectonic and chemoarchitectonic characterization of the prefrontal cortical areas in the mouse. *Brain Struct. Funct.* **214,** 339–53 (2010).

66. Niell, C., Meyer, M. & Smith, S. In vivo imaging of synapse formation on a growing dendritic arbor. *Nat. Neurosci.* **7,** 254–60 (2004).

67. Lendvai, B., Stern, E., Chen, B. & Svoboda, K. Experience-dependent plasticity of dendritic spines in the developing rat barrel cortex in vivo. *Nature* **404,** 1–6 (2000).

68. Itami, C. *et al.* Developmental Switch in Spike Timing-Dependent Plasticity at Layers 4-2/3 in the Rodent Barrel Cortex. *J. Neurosci.* **32,** 15000–15011 (2012).

69. Busetto, G., Higley, M. J. & Sabatini, B. L. Developmental presence and disappearance of postsynaptically silent synapses on dendritic spines of rat layer 2/3 pyramidal neurons. *J. Physiol.* **586,** 1519–27 (2008).

70. Akbik, F. V, Bhagat, S. M., Patel, P. R., Cafferty, W. B. J. & Strittmatter, S. M. Anatomical plasticity of adult brain is titrated by Nogo Receptor 1. *Neuron* **77,** 859–66 (2013).

71. Hensch, T. K. Critical period regulation. *Annu. Rev. Neurosci.* **27,** 549–79 (2004).

72. Budreck, E. C. & Scheiffele, P. Neuroligin-3 is a neuronal adhesion protein at GABAergic and glutamatergic synapses. *Eur. J. Neurosci.* **26,** 1738–48 (2007).

73. Cruz-Martín, A., Crespo, M. & Portera-Cailliau, C. Delayed stabilization of dendritic spines in fragile X mice. *J. Neurosci.* **30,** 7793–803 (2010).

74. Yuste, R. & Bonhoeffer, T. Genesis of dendritic spines: insights from ultrastructural and imaging studies. *Nat. Rev. Neurosci.* **5,** 24–34 (2004).

75. Yasumatsu, N., Matsuzaki, M., Miyazaki, T., Noguchi, J. & Kasai, H. Principles of long-term dynamics of dendritic spines. *J. Neurosci.* **28,** 13592–608 (2008).

76. Hill, T. C. & Zito, K. LTP-induced long-term stabilization of individual nascent dendritic spines. *J. Neurosci.* **33,** 678–86 (2013).

77. Etherton, M. *et al.* Autism-linked neuroligin-3 R451C mutation differentially alters hippocampal and cortical synaptic function. *Proc. Natl. Acad. Sci. U. S. A.* **108,** 13764–9 (2011).

78. Feldman, D. E., Nicoll, R. A. & Malenka, R. C. Synaptic plasticity at thalamocortical synapses in developing rat somatosensory cortex: LTP, LTD, and silent synapses. *J. Neurobiol.* **41,** 92–101 (1999).

79. Lu, S. M. & Lin, R. C. Thalamic afferents of the rat barrel cortex: a light- and electron-microscopic study using Phaseolus vulgaris leucoagglutinin as an anterograde tracer. *Somatosens. Mot. Res.* **10,** 1–16 (1993).

80. Yu, C., Derdikman, D., Haidarliu, S. & Ahissar, E. Parallel thalamic pathways for whisking and touch signals in the rat. *PLoS Biol.* **4,** e124 (2006).

81. Rubenstein, J. L. R. & Merzenich, M. M. Model of autism: increased ratio of excitation/inhibition in key neural systems. *Genes. Brain. Behav.* **2,** 255–67 (2003).

82. Chen, J. L. *et al.* Clustered dynamics of inhibitory synapses and dendritic spines in the adult neocortex. *Neuron* **74,** 361–73 (2012).

83. Spruston, N. Pyramidal neurons: dendritic structure and synaptic integration. *Nat. Rev. Neurosci.* **9,** 206–21 (2008).

84. Gonçalves, J. T., Anstey, J. E., Golshani, P. & Portera-Cailliau, C. Circuit level defects in the developing neocortex of Fragile X mice. *Nat. Neurosci.* **16,** 903–9 (2013).

7. Acknowledgments

I would like to express my gratitude thanks to Professor Shigeo Okabe for giving me an opportunity to be a part of this state of educational and research setup at Okabe lab and also his valuable guidance, support and encouragement throughout the tenure of my graduate studies. This work would not have been in this shape without his able and visionary advice.

I appreciate the collaborative work for research on the ASD model mice and considerate advises with Dr. Shinji Tanaka.

I am also grateful to Dr. Hirohide Iwasaki, Dr. Satoru Kondo, Dr. Ebrahimi Saman, Takahito Higashi, Yutaro Kashiwagi, Kazuki Obashi and Takao Nishiguchi for their continued support and advice. All the members of Okabe lab are acknowledged for their precious comments and helps.

This work was supported by Grant-in-Aid for JSPS Fellows.

I am sincerely thankful to my family for their support to achieve this target.

8. Figure legends

Figure 1 Spine dynamics.

A. Postnatal development of dendritic spines and PSD-95 clusters. Imaging of PSD-95-GFP (green) and DsRed2 (gray) revealed PSD-95-GFP-(+) (arrows) and PSD-95-GFP-(−) spines (arrowheads) in the SSC at different time points of postnatal development.

B. Postnatal increase of total spines and spines positive with PSD-95-GFP clusters in the SSC. Error bars indicate s.e.m of the spine densities classified as PSD-95-GFP-(+) or PSD-95-GFP-(−). P7-8: n = 3, P13-14: n = 4, P19-21: n = 4, 8 wk: n = 3.

C. *In vivo* timelapse imaging of spines at PND 20 with 24 hr interval. Gain (arrow) and loss (arrowhead) of spines were detected.

D. Turnover rates of total spines at different time points in the SSC. 2 wk: n = 6, 3 wk: n = 4, 8 wk: n = 3.

Data are presented as mean ± s.e.m. ***$P < 0.005$. Scale bars, 2 μm.

Figure 2 Comparison of two types of cranial windows.

A. Turnover rates of dendritic spines with two types of cranial windows. *In vivo* imaging was performed in the SSC at postnatal week 3 through either open- or thinned-skull windows. Spine turnover rates were comparable between two conditions, indicating minimal effects of open-skull surgery on spine dynamics. open: n = 4, thin: n = 4. Data are presented as mean ± s.e.m.

B-C. Evaluation of microglial activation after two types of surgery. Low magnification views of brain sections (upper) after thinned-skull preparation (B) and open-skull preparation (C). Brain sections containing pyramidal neurons expressing DsRed2 (red) using in utero electroporation were immunostained with Iba-1 antibody (green). High magnification views of Iba-1 immunostaining of boxed regions in upper panels were shown in lower. Scale bars, 500 µm for upper panels; 50 µm for lower.

Figure 3 Classification of spine by PSD-95 and spine containing PSD-95 dynamics

A. *In vivo* imaging of PSD-95-GFP (gray in middle panels, green in right panels) and dendrites filled with DsRed2 (gray) at PND 14 in the SSC. Gain (arrows) and loss (arrowheads) of PSD-95-GFP-(+) spines were detected.

B. The frequency distribution of G_{shaft}/R_{shaft} at randomly selected positions of dendritic shafts from the data of in vivo imaging with an ICR mouse at postnatal week 2 (n = 196). Red line and dashed lines indicated the average and the twice and half of that. More than 95% of them were in the area between dashed lines.

C. Distribution of spine volumes classified by the presence or absence of PSD-95-GFP clusters. PSD-95-(+) spines: n = 353, PSD-95-(−) spines: n = 43.

D. Gain and loss of spines classified by the presence or absence of PSD-95-GFP clusters at three different time points during postnatal development.

E. Increase in total spines and PSD-95-GFP (+) spines estimated from *in vivo* imaging at postnatal 2 weeks (lines) compared with the actual increase of spine density.

Data are presented as mean ± s.e.m. *P < 0.05, ***P < 0.005. Scale bars, 2 μm.

Figure 4 Selective regulation of PSD-95-GFP (+) spine formation by sensory stimuli.

A. Gain and loss of spines classified by the presence or absence of PSD-95-GFP clusters in control or whisker-trimmed mice. Control: n = 3, trimming: n = 3.

B. Density of PSD-95-GFP (+) and (-) spines in the SSC after repetitive whisker trimming from PND 14 to 21. Control: n = 5, trimming: n = 4.

Data are presented as mean ± s.e.m. *P < 0.05, ***P < 0.005.

Figure 5 Characterization of gephyrin-GFP-(+) and (−) spines.

A. *In vivo* imaging of gephyrin-GFP (gray in middle panels, green in right panels) and DsRed2 (gray) revealed that gephyrin-GFP localized on dendritic shafts (arrows) and spines (arrowhead) in layer 2/3 pyramidal neurons in SSC.

B. VGluT1 or VGluT2 (middle, green; lower, blue) immunocytochemistry of the SSC containing neurons expressing DsRed2 (magenta) and gephyrin-GFP (green) by in utero electroporation. Open arrow; Gephyrin-GFP-(+) spine without a contact with VGluT1 puncta. Solid arrows; Gephyrin-GFP-(+) spines juxtaposed to VGluT2 puncta. Open arrowheads; Gephyrin-GFP-(−) spines without contacts with VGluT2 puncta. Sold arrowhead; Gephyrin-GFP-(−) spine juxtaposed to VGluT1 punctum.

C. Percentage of gephyrin-GFP-(+) or (−) spines in close apposition to VGluT1 and VGluT2 puncta. To estimate the apposition of fluorescent puncta at chance level, the GFP channel was shifted by 50 pixels (pixel shift) and the percentage of apposition was calculated (VGluT1, n = 239 spines; VGluT2, n = 270 spines).

D. Gephyrin (middle, green; lower, blue) immunocytochemistry of the SSC containing neurons expressing DsRed2 (magenta) and PSD-95-GFP (green) by in utero electroporation. Arrow; PSD-95-GFP (+) spine juxtaposed to gephyrin puncta.

E. Percentage of gephyrin puncta (+) or (-) spines containing PSD-95-GFP (n = 247 spines).

F. Densities of dendritic spines, shaft gephyrin, and spine gephyrin clusters per unit length of dendrites in the SSC (n = 5).

G. Distribution of spine volumes classified by the presence or absence of gephyrin-GFP clusters. Gephyrin-GFP-(+) spines: n = 80, gephyrin-GFP-(−) spines: n = 337.

Data are presented as mean ± s.e.m. Scale bars, 3 μm.

Figure 6 Dynamics of Spines classified by the presence or absence of gephyrin-GFP.

A. *In vivo* imaging of gephyrin-GFP (green) and dendrites filled with DsRed2 (gray). Gain (arrow) and loss (arrowheads) of gephyrin-GFP-(−) spines were detected.

B. Spines were classified by the presence or absence of gephyrin-GFP, and the rates of gain and loss of spines per unit length of dendrites were measured (n = 5).

Data are presented as mean ± s.e.m.

Figure 7 Histological analysis of the cortical architecture in ASD mouse models.

A, B. Lower (A) and higher (B) magnification views of the SSC of C57Bl/6J, patDp/+, NLG R451C and BTBR mice. Nissl staining of 50 μm thick vibratome sections.

C, D. Lower (C) and higher (D) magnification views of the AFC of C57Bl/6J, patDp/+,NLG R451C and BTBR mice. Nissl staining of 50 µm thick vibratome sections.

Scale bars, 500 µm for A and C; 200 µm for B and D.

Figure 8 Upregulation of synapse turnover in patDp/+ mice.

A. *In vivo* imaging of PSD-95-GFP (green) and dendrites filled with DsRed2 (gray) in the SSC of patDp/+ mice. Loss of PSD-95-GFP-(+) spines was detected (arrowheads).

B. Spine density with or without PSD-95-GFP clusters in the SSC of wild-type and patDp/+ mice. Error bars indicate s.e.m of the spine densities classified as PSD-95-GFP-(+) or PSD-95-GFP-(−).

C. Turnover of PSD-95-GFP-(+) and (−) spines over 2 days in the SSC of wild-type and patDp/+ mice.

D. Gain and loss of PSD-95-GFP-(+) and (−) spines per unit length of dendrites over 2 days in the SSC of wild-type and patDp/+ mice.

E. *In vivo* imaging of gephyrin-GFP (green) and dendrites filled with DsRed2 (gray). Gain (arrow) and loss (arrowheads) of spines were detected.

F. Spine density with or without gephyrin-GFP clusters in the SSC of wild-type and patDp/+ mice. Error bars indicate the s.e.m of the spine densities classified as gephyrin-GFP-(+) or gephyrin-GFP-(−).

G. Turnover of gephyrin-GFP-(+) and (−) spines over 2 days in the SSC of wild-type and patDp/+ mice.

H. Gain and loss of gephyrin-GFP-(+) and (−) spines per unit length of dendrites over 2 days in the SSC of wild-type and patDp/+ mice.

B-D, WT: n = 4, patDp/+: n = 4. F-H, WT: n = 5, patDp/+: n = 5. Data are presented as mean ± s.e.m. $*P < 0.05$, $**P < 0.01$, $***P < 0.005$. Scale bars, 3 μm.

Figure 9 PatDp/+ mice show enhanced spine dynamics in the AFC at postnatal week 3.

A. A spread of imaging sites on the dorsal surface of the cortex. The red striped area included 108 imaging sites from 27 independent experiments (6 patDp/+ mice, 6 NLG R451C mice, 3 BTBR mice, and 12 control mice).

B, C. Diagrams of coronal sections at the levels of B and C in the map shown in (A). The red striped areas corresponded to the imaging sites. The imaging sites were rostral to the primary motor cortex and were outside of the lateral border of the prefrontal cortex.

D. *In vivo* time-lapse imaging of PSD-95-GFP (green) and dendrites filled with DsRed2 (gray) over 2 days in the AFC of wild-type and patDp/+ mice. Gain (arrow) and loss (arrowhead) of PSD-95-GFP-(+) spines were detected.

E. Spine density with or without PSD-95-GFP clusters in the AFC of wild-type and patDp/+ mice. Error bars indicate the s.e.m of the spine densities classified as PSD-95-GFP-(+) or PSD-95-GFP-(−).

F. Turnover of PSD-95-GFP-(+) and (−) spines over 2 days in the AFC of wild-type and patDp/+ mice at postnatal week 3.

G. Gain and loss of PSD-95-GFP-(+) and (−) spines per unit length of dendrites in the AFC of wild-type and patDp/+ mice at postnatal week 3.

E-G, WT: n = 5, patDp/+: n = 6. Data are presented as mean ± s.e.m. *P < 0.05, ***P < 0.005. Scale bar, 1 mm for A, 3 μm for D.

Figure 10 PatDp/+ mice show enhanced spine dynamics in the SSC at postnatal week 2.

A. *In vivo* time-lapse imaging of PSD-95-GFP (green) and dendrites filled with DsRed2 (gray) in the SSC of wild-type and patDp/+ mice at postnatal week 2. Gain (arrows) and loss (arrowhead) of spines were detected.

B. Spine density with or without PSD-95-GFP clusters in the SSC of wild-type and patDp/+ mice at postnatal week 2. Error bars indicate the s.e.m of the spine densities classified as gephyrin-GFP-(+) or gephyrin-GFP-(−).

C. Turnover of PSD-95-GFP-(+) and (−) spines over 1 day in the SSC of wild-type and patDp/+ mice at postnatal week 2.

D. Gain and loss of PSD-95-GFP-(+) and (−) spines per unit length of dendrites in the SSC of wild-type and patDp/+ mice at postnatal week 2.

B-D, WT: n = 5, patDp/+: n = 4. Data are presented as mean ± s.e.m. $*P < 0.05$, $***P < 0.005$. Scale bars, 3 μm.

Figure 11 Upregulation of spine turnover in NLG R451C mice.

A. In vivo time-lapse imaging of PSD-95-GFP (green) and dendrites filled with DsRed2 (gray) over 2 days in the AFC of wild-type and NLG R451C mice. Loss (arrowhead) of PSD-95-GFP-(+) spines was detected.

B. Spine density with or without PSD-95-GFP clusters in the AFC of wild-type and NLG R451C mice. Error bars indicate the s.e.m of the spine densities classified as PSD-95-GFP-(+) or PSD-95-GFP-(−).

C. Turnover of PSD-95-GFP-(+) and (−) spines over 2 days in the AFC of wild-type and NLG R451C mice.

D. Gain and loss of PSD-95-GFP-(+) and (−) spines per unit length of dendrites over 2 days in the AFC of wild-type and NLG R451C mice.

E. *In vivo* time-lapse imaging of gephyrin-GFP (green) and dendrites filled with DsRed2 (gray) over 2 days in the SSC of wild-type and NLG R451C mice. Gain (arrows) and loss (arrowheads) of gephyrin-GFP-(−) spines were detected.

F. Spine density with or without gephyrin-GFP clusters in the SSC of wild-type and NLG R451C mice. Error bars indicate the s.e.m of the spine densities classified as gephyrin-GFP-(+) or gephyrin-GFP-(−).

G. Turnover of gephyrin-GFP-(+) and (−) spines over 2 days in the SSC of wild-type and NLG R451C mice.

H. Gain and loss of gephyrin-GFP-(+) and (−) spines per unit length of dendrites over 2 days in the SSC of wild-type and NLG R451C mice.

B-D, WT: n = 4, R451C: n = 6. F-G, WT: n = 4, R451C: n = 6. Data are presented as mean ± s.e.m. $^*P < 0.05$, $^{**}P < 0.01$. Scale bars, 3 μm.

Figure 12 Altered dynamics of PSD-95-GFP-(+) spines in the AFC of BTBR mice.

A, B. Turnover rates of PSD-95-GFP-(+) and (−) spines (A) and gain and loss of PSD-95-GFP-(+) and (−) spines per unit length of dendrites (B) over 2 days in the AFC of C57Bl/6J and BTBR mice.

A-B, C57Bl/6: n = 3, BTBR: n = 3. Data are presented as mean ± s.e.m. $^*P < 0.05$, $^{***}P < 0.005$.

Figure 13 Dynamics of shaft and spine gephyrin clusters in patDp/+ mice and NLG R451C mice.

A. Density of gephyrin clusters on dendritic shafts in the SSC of wild-type and patDp/+ mice.

B. Gain and loss of gephyrin clusters on dendritic shafts in the SSC of wild-type and patDp/+ mice.

C. Gain and loss of gephyrin clusters on dendritic spines in the SSC of wild-type and patDp/+ mice.

D. Density of gephyrin clusters on dendritic shafts in the SSC of wild-type and NLG R451C mice.

E. Gain and loss of gephyrin clusters on dendritic shafts in the SSC of wild-type and NLG R451C mice.

F. Gain and loss of gephyrin clusters on dendritic spines in the SSC of wild-type and NLG R451C mice.

A-C, WT: n = 5, patDp/+: n = 5. D-F, WT: n = 4, R451C: n = 6. Data are presented as mean ± s.e.m. *P < 0.05.

Figure 14 Distinct turnover rates and cluster intensities between shaft and spine gephyrin clusters.

A. Gain and loss of shaft and spine gephyrin clusters. Elimination rate of spine gephyrin clusters was significantly higher than that of shaft gephyrin clusters.

B. Relative intensities of shaft and spine gephyrin clusters were calculated by normalizing the total intensity of each gephyrin cluster to the average intensities of all gephyrin clusters in each dendritic segment. Relative intensities of spine gephyrin clusters were significantly lower than those of shaft gephyrin clusters.

A-B, n = 5. Data are presented as mean ± s.e.m. *P < 0.05, ***P < 0.005.

Figure 15 Dendritic spines within 4 µm from shaft gephyrin clusters showed higher elimination rate in wild-type mice but not in patDp/+ and NLG R451C mice.

A. Elimination rate of spines near (0–4 µm) and away (>4 µm) from shaft gephyrin clusters in wild-type and patDp/+ mice.

B. Elimination rate of spines near (0–4 µm) and away (>4 µm) from shaft gephyrin clusters in wild-type and NLG R451C mice.

A, WT: n = 5, patDp/+: n = 5. B, WT: n = 4, R451C: n = 6. Data are presented as mean ± s.e.m. $^{*}P < 0.05$ in Wilcoxon signed-rank test (A) and paired t-test (B).

9. Figures

Figure 1

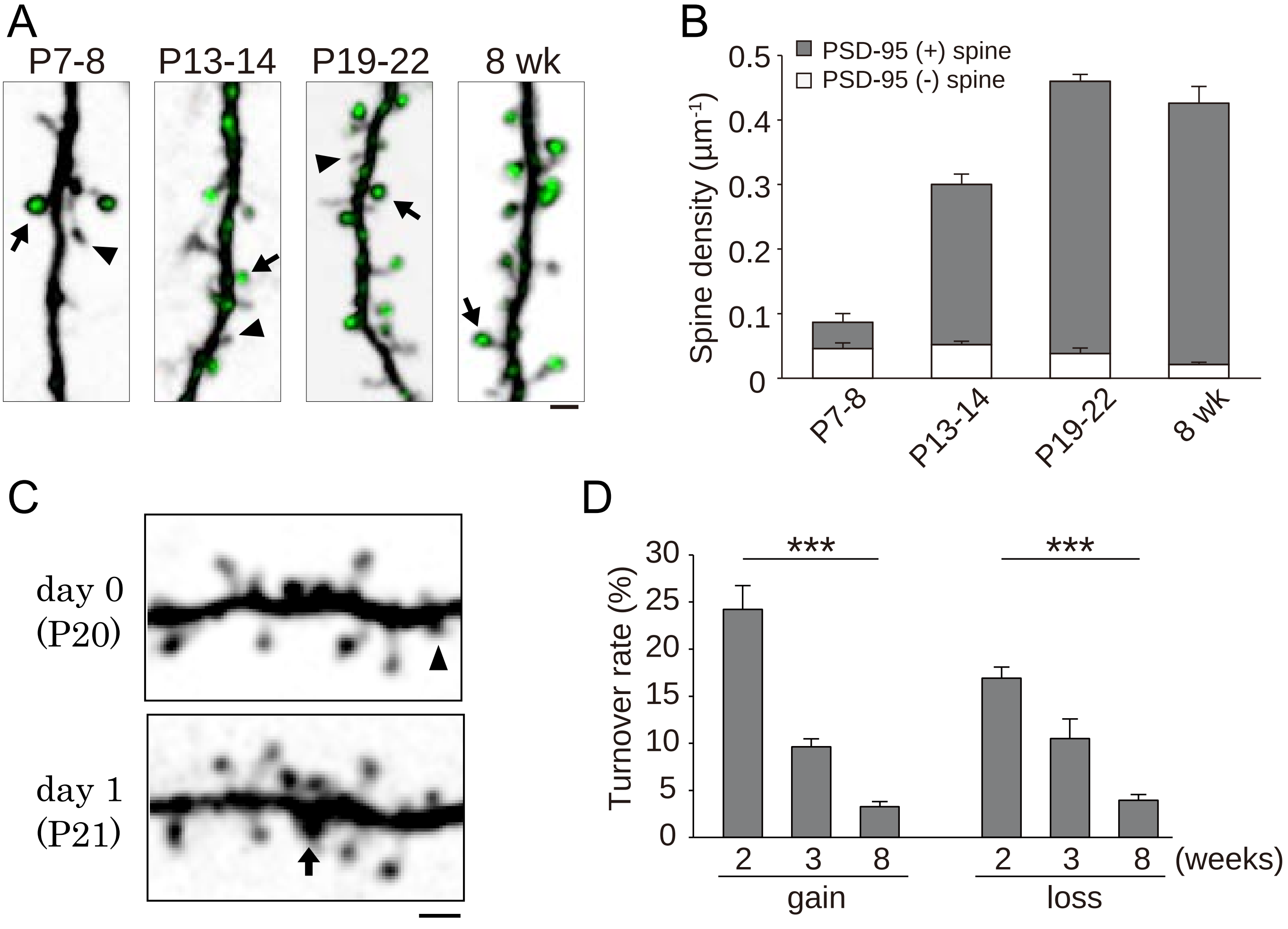

Figure 2

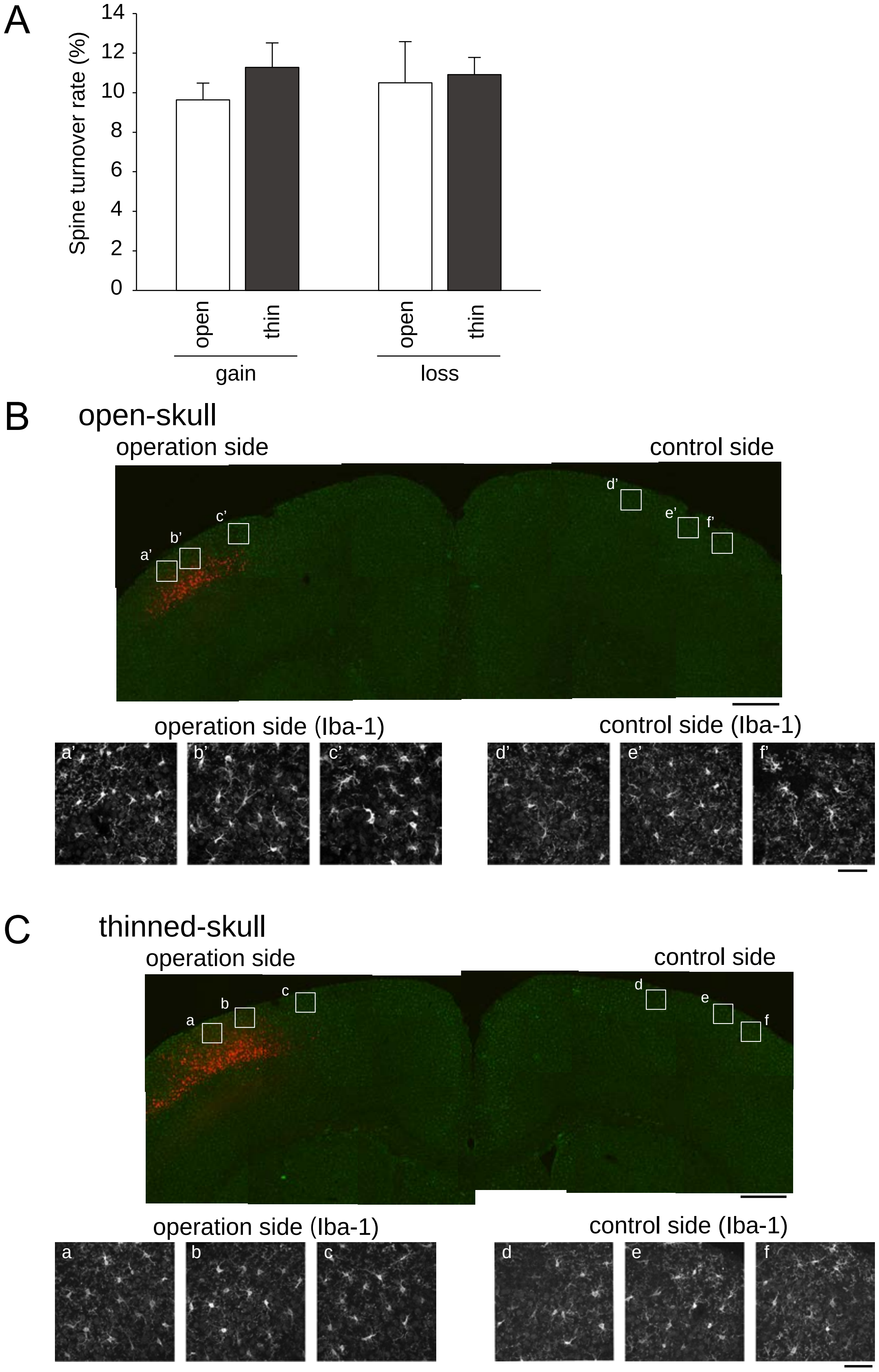
A
Spine turnover rate (%)
14
12
10
8
6
4
2
0
open
thin
gain
open
thin
loss
B
open-skull
operation side
control side
a'
b'
c'
d'
e'
f'
operation side (Iba-1)
control side (Iba-1)
a'
b'
c'
d'
e'
f'
C
thinned-skull
operation side
control side
a
b
c
d
e
f
operation side (Iba-1)
control side (Iba-1)
a
b
c
d
e
f

Figure 3

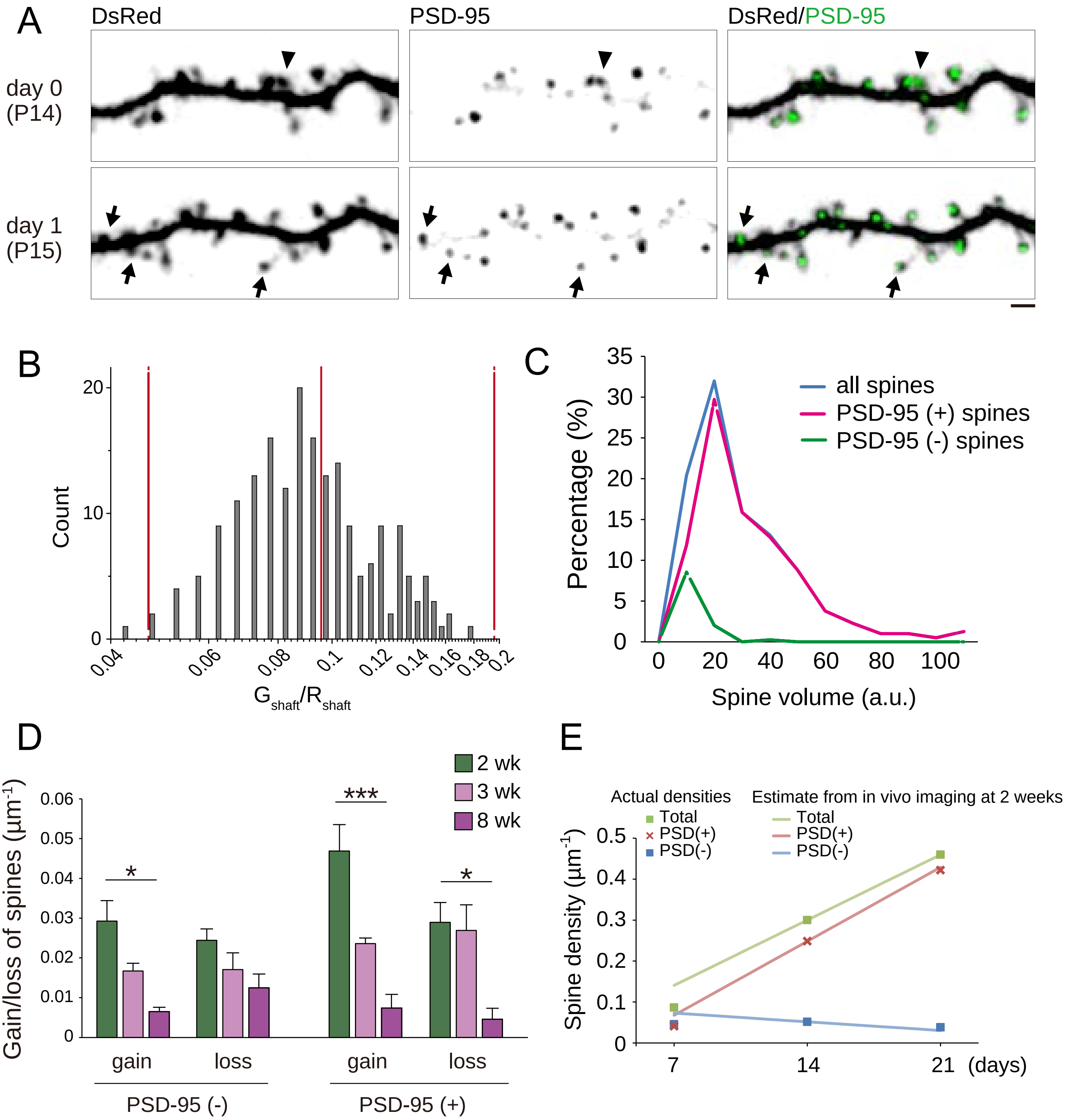
A
DsRed
PSD-95
DsRed/PSD-95
day 0
(P14)
day 1
(P15)
B
Count
20
10
0
0.04
0.06
0.08
0.1
0.12
0.14
0.16
0.18
0.2
G_{shaft}/R_{shaft}
C
Percentage (%)
35
30
25
20
15
10
5
0
0
20
40
60
80
100
Spine volume (a.u.)
all spines
PSD-95 (+) spines
PSD-95 (-) spines
D
Gain/loss of spines (μm^{-1})
0.06
0.05
0.04
0.03
0.02
0.01
0
*
***
*
2 wk
3 wk
8 wk
gain
loss
gain
loss
PSD-95 (-)
PSD-95 (+)
E
Actual densities
Total
PSD(+)
PSD(-)
Estimate from in vivo imaging at 2 weeks
Total
PSD(+)
PSD(-)
Spine density (μm^{-1})
0.5
0.4
0.3
0.2
0.1
0
7
14
21 (days)

Figure 4

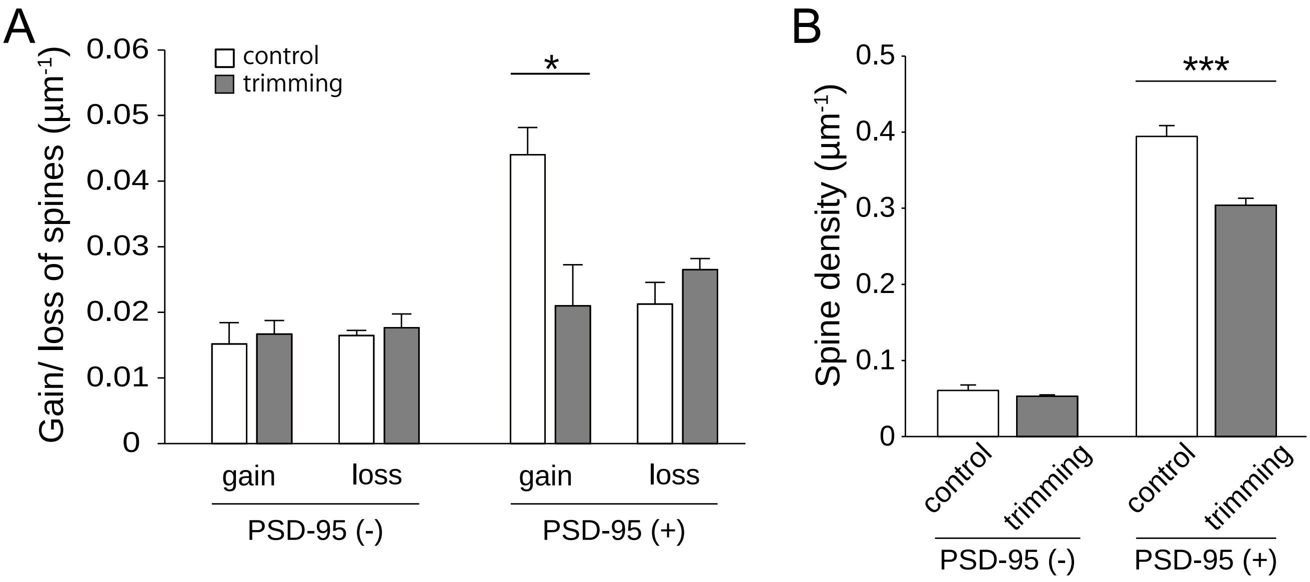
A
Gain/ loss of spines (µm-1)
0.06
0.05
0.04
0.03
0.02
0.01
0
□ control
▨ trimming
*
gain
loss
gain
loss
PSD-95 (-)
PSD-95 (+)
B
Spine density (µm-1)
0.5
0.4
0.3
0.2
0.1
0
***
control
trimming
control
trimming
PSD-95 (-)
PSD-95 (+)

Figure 5

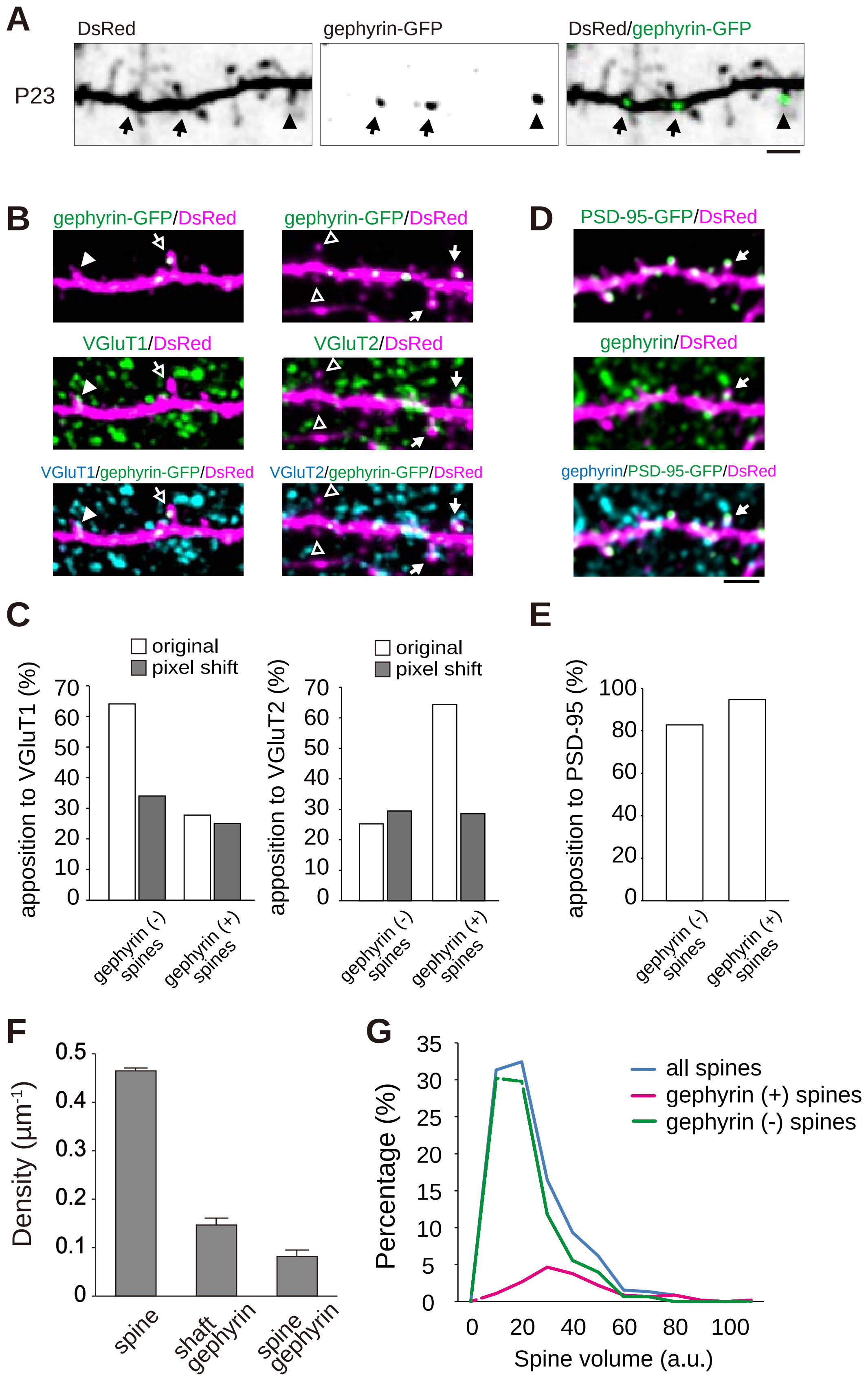
A
DsRed
gephyrin-GFP
DsRed/gephyrin-GFP
P23
B
gephyrin-GFP/DsRed
gephyrin-GFP/DsRed
VGluT1/DsRed
VGluT2/DsRed
VGluT1/gephyrin-GFP/DsRed
VGluT2/gephyrin-GFP/DsRed
D
PSD-95-GFP/DsRed
gephyrin/DsRed
gephyrin/PSD-95-GFP/DsRed
C
☐ original
▨ pixel shift
apposition to VGluT1 (%)
0
10
20
30
40
50
60
70
gephyrin (-) spines
gephyrin (+) spines
☐ original
▨ pixel shift
apposition to VGluT2 (%)
0
10
20
30
40
50
60
70
gephyrin (-) spines
gephyrin (+) spines
E
apposition to PSD-95 (%)
0
20
40
60
80
100
gephyrin (-) spines
gephyrin (+) spines
F
Density (μm⁻¹)
0
0.1
0.2
0.3
0.4
0.5
spine
shaft gephyrin
spine gephyrin
G
Percentage (%)
0
5
10
15
20
25
30
35
0
20
40
60
80
100
Spine volume (a.u.)
all spines
gephyrin (+) spines
gephyrin (-) spines

Figure 6

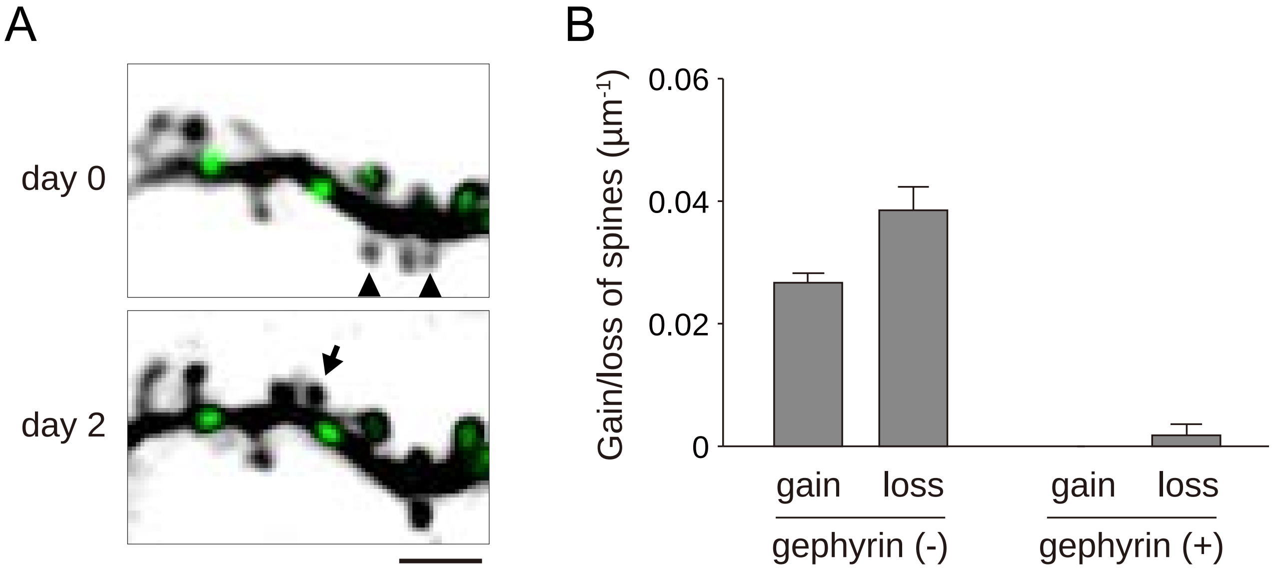
A
day 0
day 2
B
Gain/loss of spines (μm^{-1})
0.06
0.04
0.02
0
gain
loss
gephyrin (-)
gain
loss
gephyrin (+)

Figure 7

Somatosensory cortex

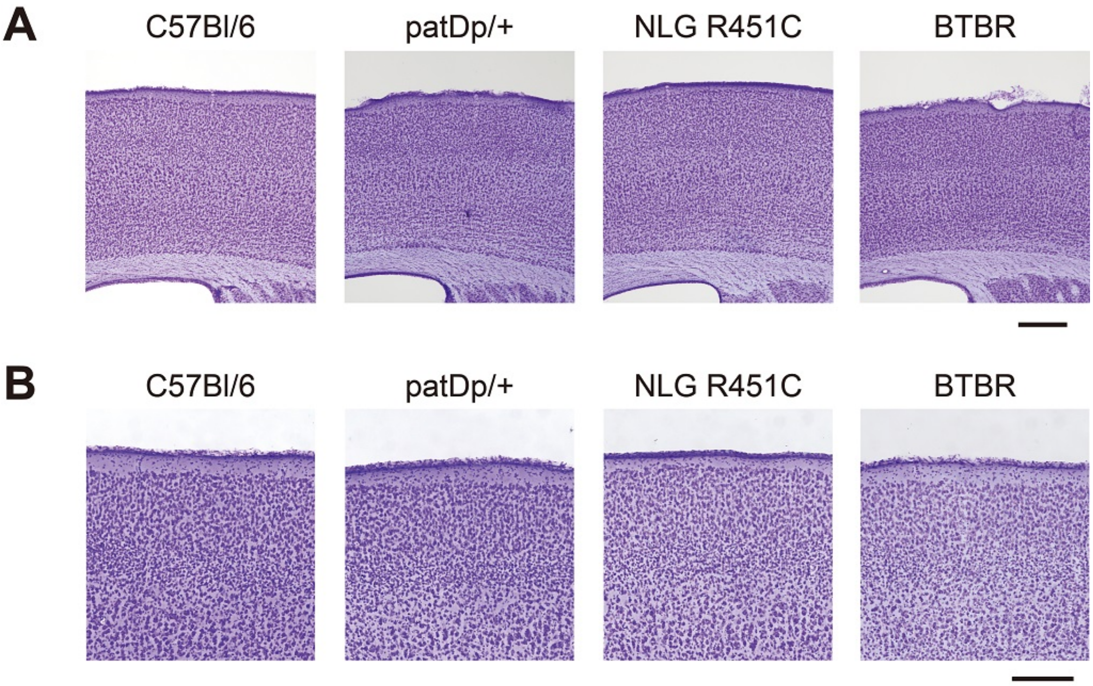

Anterior frontal cortex

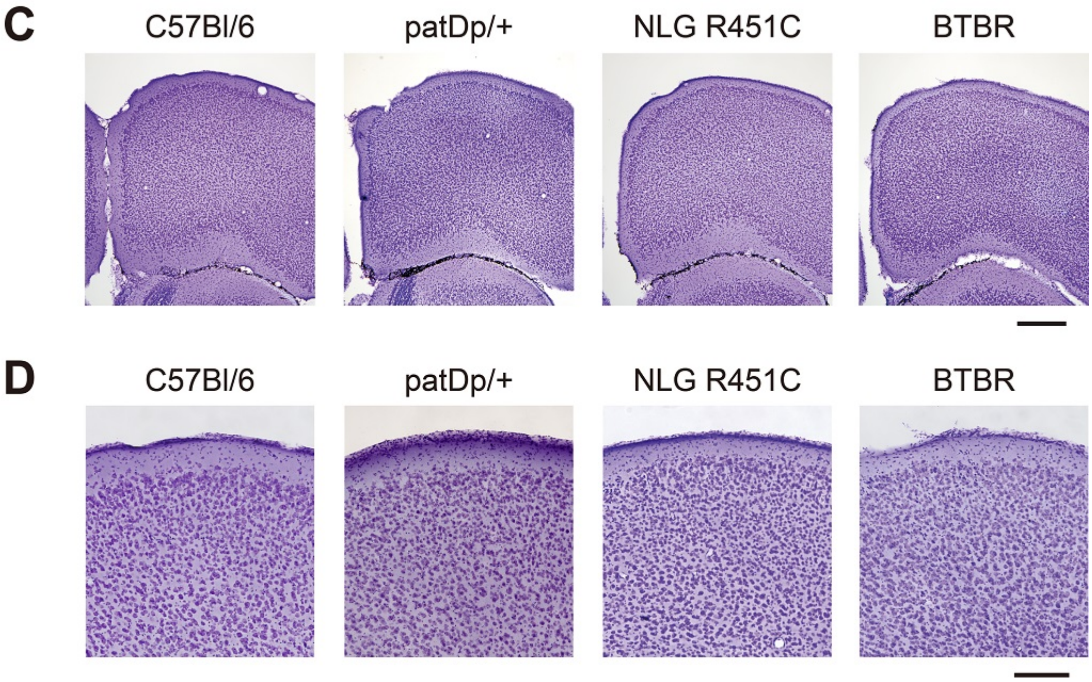

Figure 8

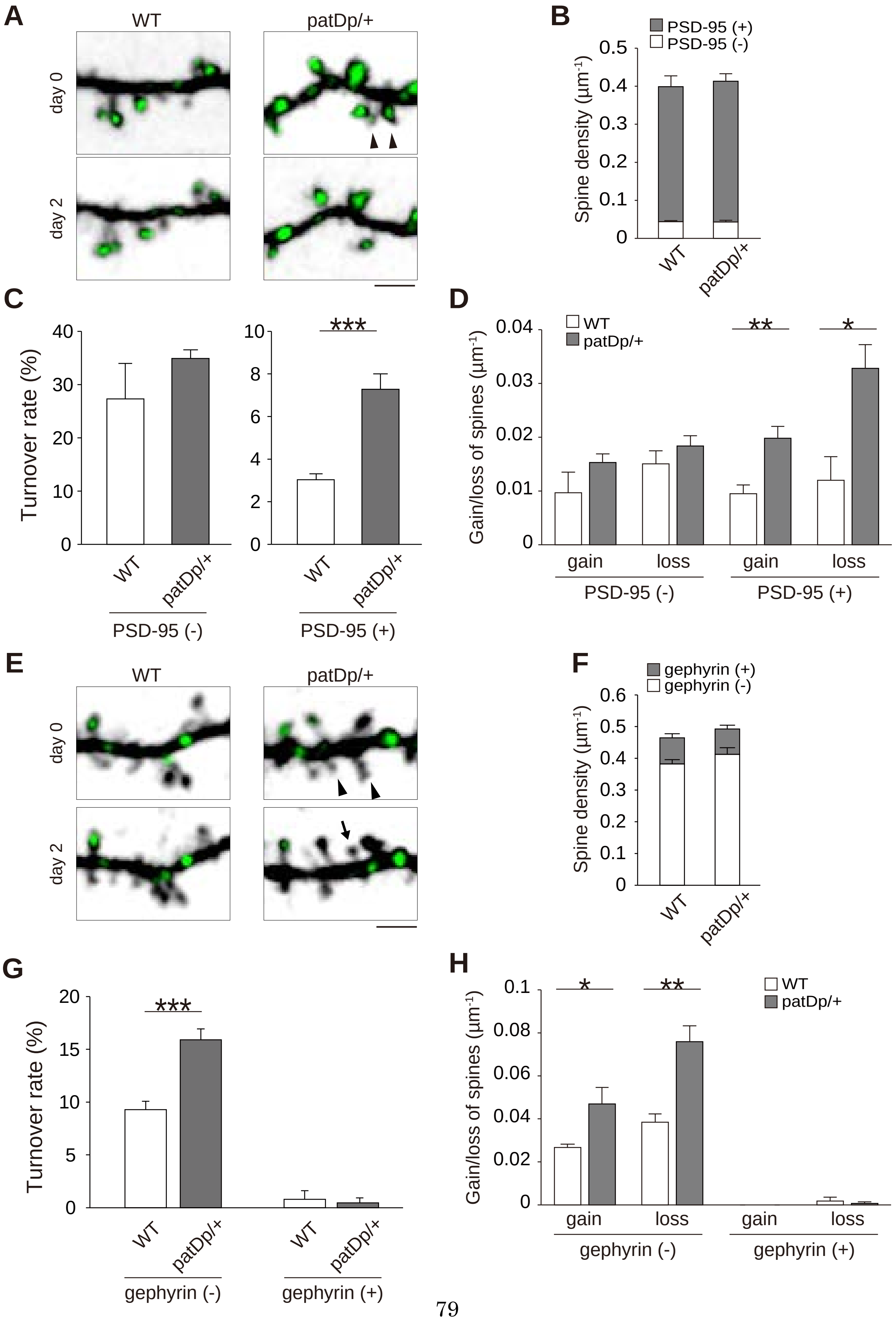
A
WT
patDp/+
day 0
day 2
B
■ PSD-95 (+)
□ PSD-95 (-)
Spine density (μm⁻¹)
0
0.1
0.2
0.3
0.4
0.5
WT
patDp/+
C
Turnover rate (%)
0
10
20
30
40
WT
patDp/+
PSD-95 (-)
0
2
4
6
8
10
***
WT
patDp/+
PSD-95 (+)
D
□ WT
■ patDp/+
Gain/loss of spines (μm⁻¹)
0
0.01
0.02
0.03
0.04
**
*
gain
loss
gain
loss
PSD-95 (-)
PSD-95 (+)
E
WT
patDp/+
day 0
day 2
F
■ gephyrin (+)
□ gephyrin (-)
Spine density (μm⁻¹)
0
0.1
0.2
0.3
0.4
0.5
0.6
WT
patDp/+
G
Turnover rate (%)
0
5
10
15
20
***
WT
patDp/+
WT
patDp/+
gephyrin (-)
gephyrin (+)
H
□ WT
■ patDp/+
Gain/loss of spines (μm⁻¹)
0
0.02
0.04
0.06
0.08
0.1
*
**
gain
loss
gain
loss
gephyrin (-)
gephyrin (+)

Figure 9

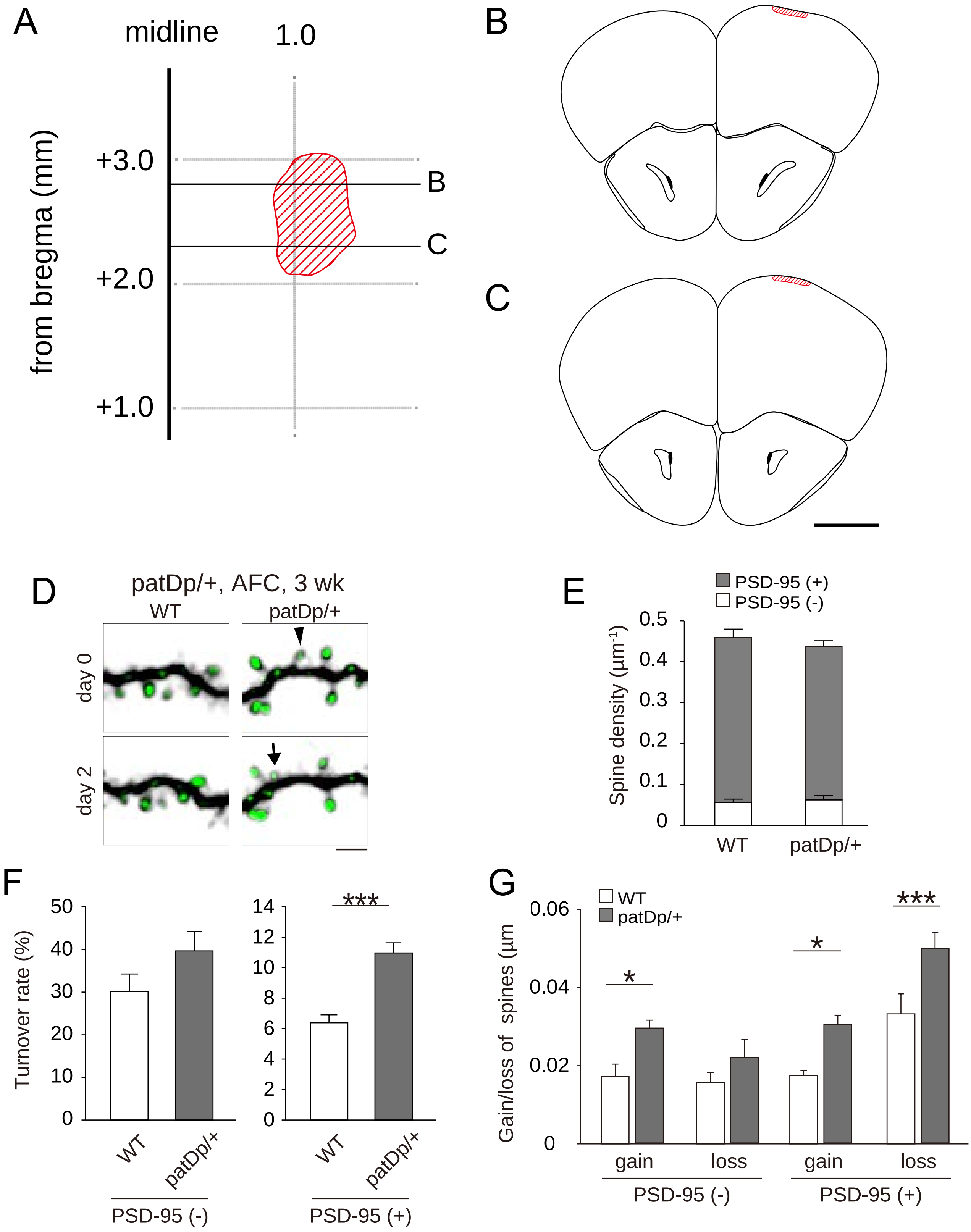
A
midline
1.0
from bregma (mm)
+3.0
+2.0
+1.0
B
C
B
C
D
patDp/+, AFC, 3 wk
WT
patDp/+
day 0
day 2
E
PSD-95 (+)
PSD-95 (-)
Spine density (µm^{-1})
0.5
0.4
0.3
0.2
0.1
0
WT
patDp/+
F
Turnover rate (%)
50
40
30
20
10
0
WT
patDp/+
PSD-95 (-)
14
12
10
8
6
4
2
0
***
WT
patDp/+
PSD-95 (+)
G
WT
patDp/+
Gain/loss of spines (µm
0.06
0.04
0.02
0
*
*
***
gain
loss
gain
loss
PSD-95 (-)
PSD-95 (+)

Figure 10

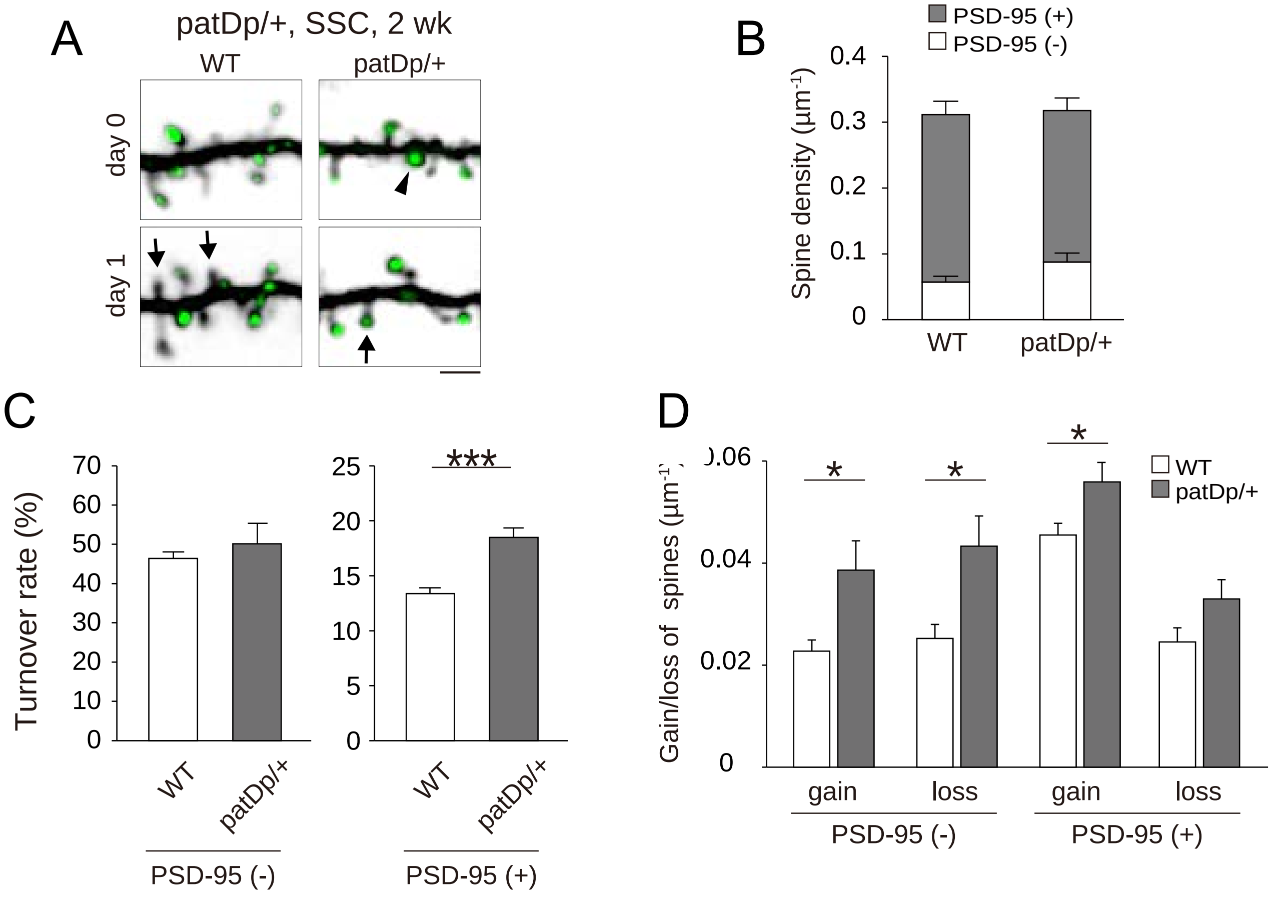

A
patDp/+, SSC, 2 wk
WT
patDp/+
day 0
day 1
B
PSD-95 (+)
PSD-95 (-)
Spine density (μm^{-1})
0.4
0.3
0.2
0.1
0
WT
patDp/+
C
Turnover rate (%)
70
60
50
40
30
20
10
0
WT
patDp/+
PSD-95 (-)
***
25
20
15
10
5
0
WT
patDp/+
PSD-95 (+)
D
Gain/loss of spines (μm^{-1})
.06
0.04
0.02
0
*
*
*
WT
patDp/+
gain
loss
gain
loss
PSD-95 (-)
PSD-95 (+)

Figure 11

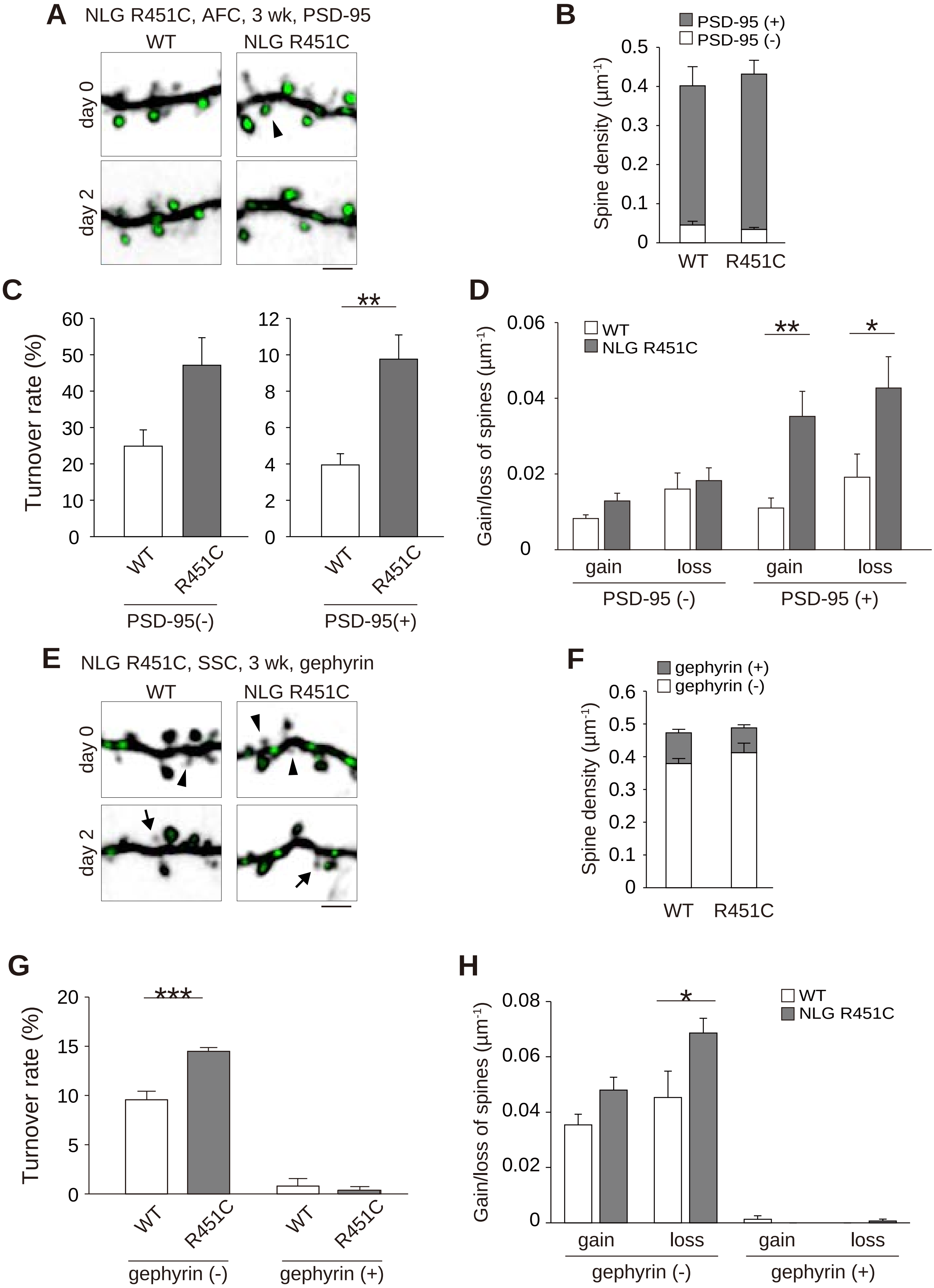
A
NLG R451C, AFC, 3 wk, PSD-95
WT
NLG R451C
day 0
day 2
B
PSD-95 (+)
PSD-95 (-)
Spine density (μm^{-1})
0.5
0.4
0.3
0.2
0.1
0
WT
R451C
C
Turnover rate (%)
60
50
40
30
20
10
0
WT
R451C
PSD-95(-)
12
10
8
6
4
2
0
**
WT
R451C
PSD-95(+)
D
Gain/loss of spines (μm^{-1})
0.06
0.04
0.02
0
WT
NLG R451C
**
*
gain
loss
gain
loss
PSD-95 (-)
PSD-95 (+)
E
NLG R451C, SSC, 3 wk, gephyrin
WT
NLG R451C
day 0
day 2
F
gephyrin (+)
gephyrin (-)
Spine density (μm^{-1})
0.6
0.5
0.4
0.3
0.2
0.1
0
WT
R451C
G
Turnover rate (%)
20
15
10
5
0
***
WT
R451C
WT
R451C
gephyrin (-)
gephyrin (+)
H
Gain/loss of spines (μm^{-1})
0.08
0.06
0.04
0.02
0
*
WT
NLG R451C
gain
loss
gain
loss
gephyrin (-)
gephyrin (+)

Figure 12

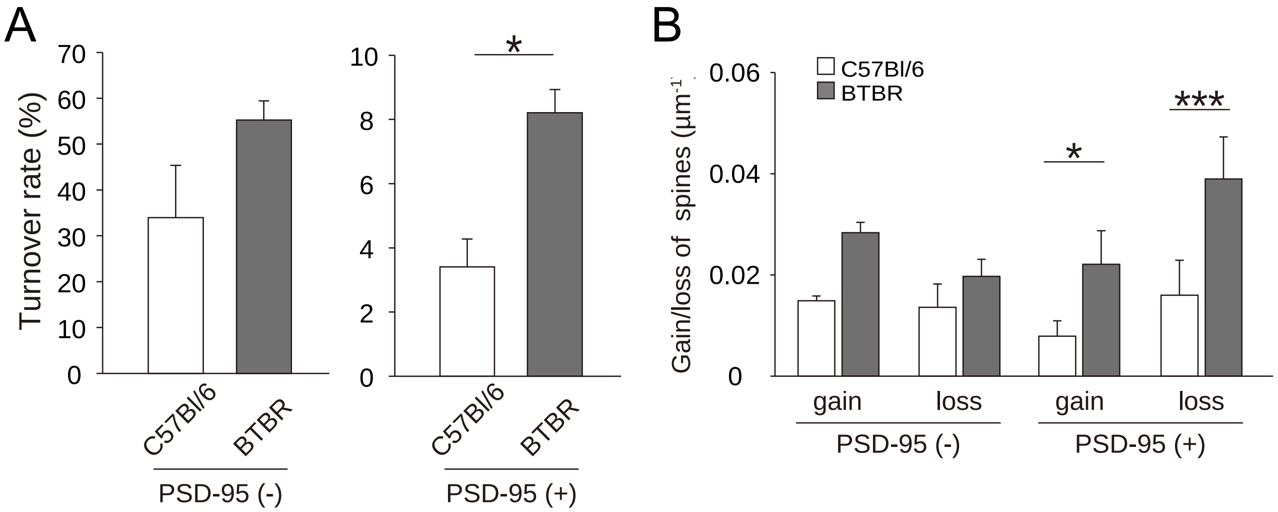
A
70
60
50
40
30
20
10
0
Turnover rate (%)
C57Bl/6
BTBR
PSD-95 (-)
10
8
6
4
2
0
*
C57Bl/6
BTBR
PSD-95 (+)
B
0.06
0.04
0.02
0
Gain/loss of spines (μm-1)
□ C57Bl/6
■ BTBR
*
***
gain
loss
gain
loss
PSD-95 (-)
PSD-95 (+)

Figure 13

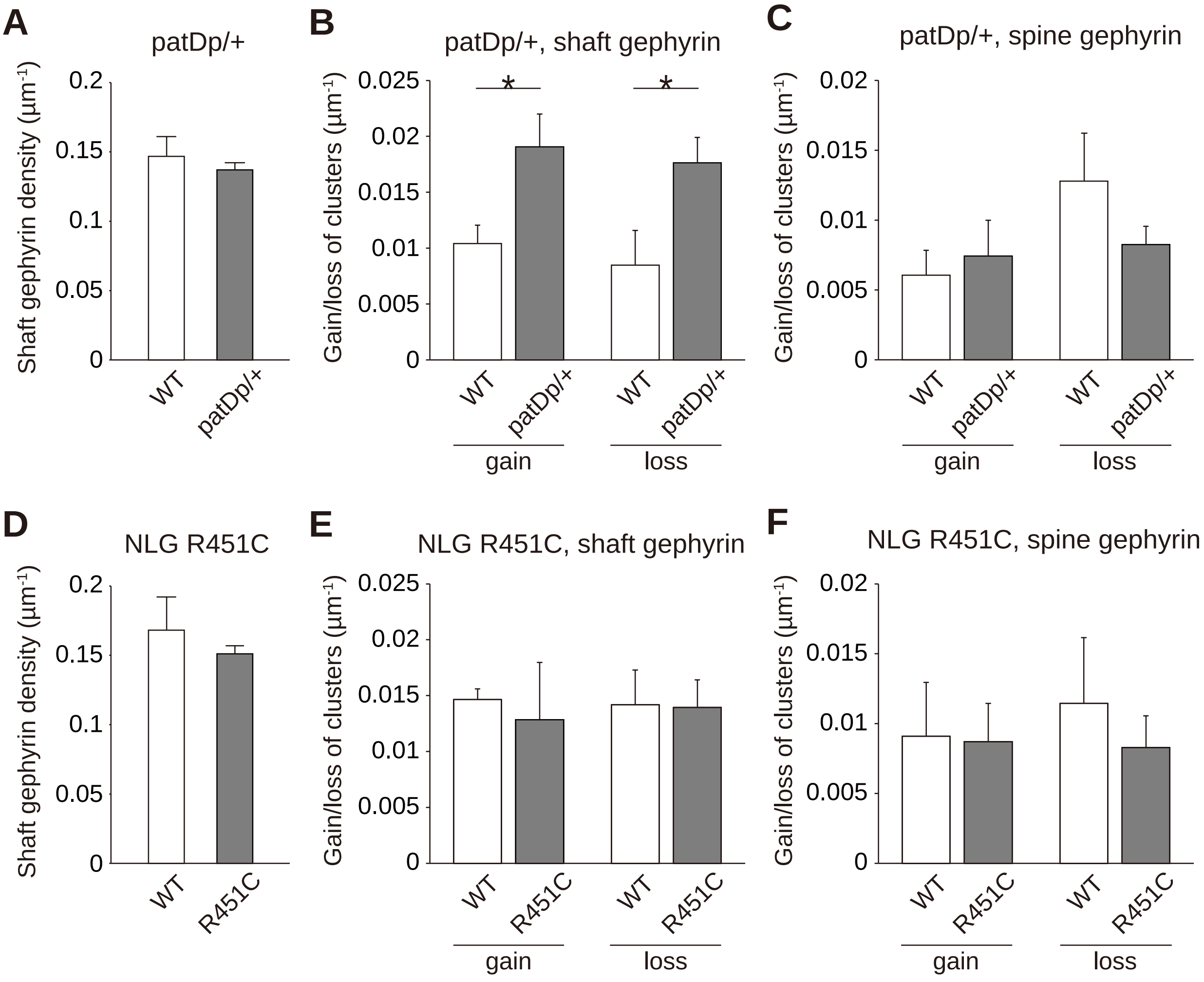
A
patDp/+
Shaft gephyrin density (µm-1)
0.2
0.15
0.1
0.05
0
WT
patDp/+
B
patDp/+, shaft gephyrin
Gain/loss of clusters (µm-1)
0.025
0.02
0.015
0.01
0.005
0
*
*
WT
patDp/+
WT
patDp/+
gain
loss
C
patDp/+, spine gephyrin
Gain/loss of clusters (µm-1)
0.02
0.015
0.01
0.005
0
WT
patDp/+
WT
patDp/+
gain
loss
D
NLG R451C
Shaft gephyrin density (µm-1)
0.2
0.15
0.1
0.05
0
WT
R451C
E
NLG R451C, shaft gephyrin
Gain/loss of clusters (µm-1)
0.025
0.02
0.015
0.01
0.005
0
WT
R451C
WT
R451C
gain
loss
F
NLG R451C, spine gephyrin
Gain/loss of clusters (µm-1)
0.02
0.015
0.01
0.005
0
WT
R451C
WT
R451C
gain
loss

Figure 14

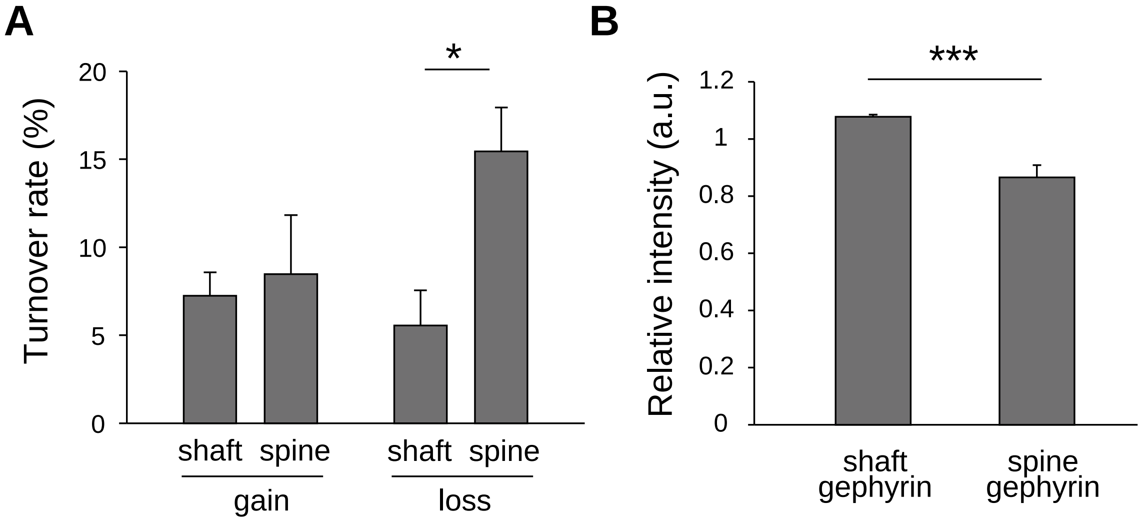
A
B
*
20
15
10
5
0
Turnover rate (%)
shaft
spine
shaft
spine
gain
loss
***
1.2
1
0.8
0.6
0.4
0.2
0
Relative intensity (a.u.)
shaft gephyrin
spine gephyrin

Figure 15

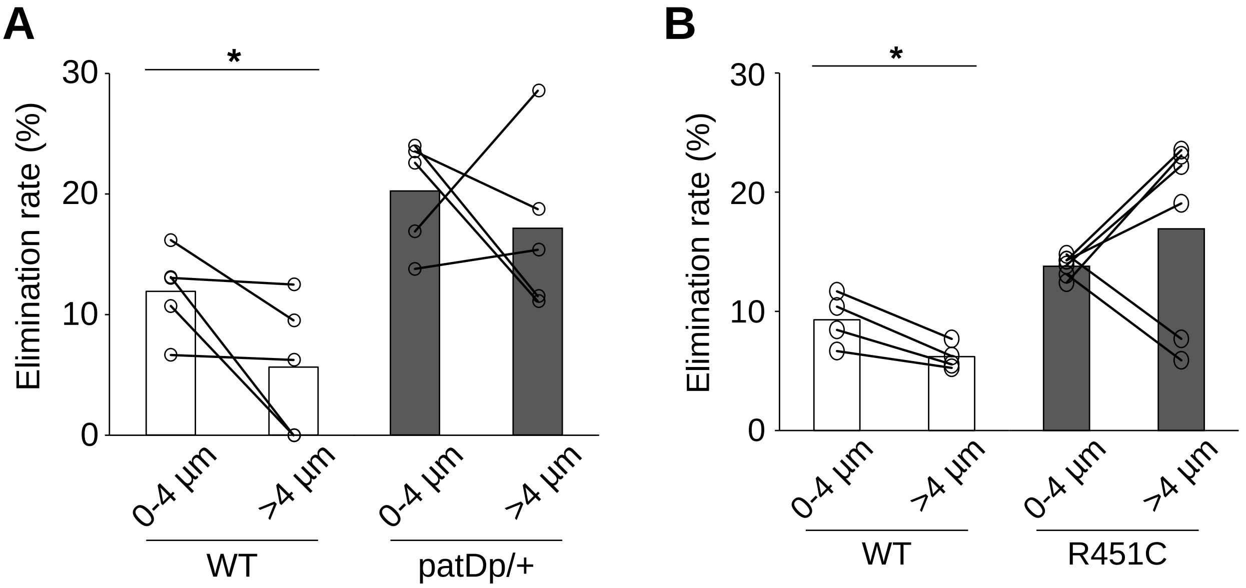
A
*
30
20
10
0
Elimination rate (%)
0-4 µm
>4 µm
0-4 µm
>4 µm
WT
patDp/+
B
*
30
20
10
0
Elimination rate (%)
0-4 µm
>4 µm
0-4 µm
>4 µm
WT
R451C